

The mineralization process of the Lanuoma Pb-Zn-Sb deposit in the Sanjiang Tethys region: Constraints from in situ sulfur isotopes and trace element compositions



Xiangyuan Sheng^{a,b}, Xianwu Bi^{a,*}, Ruizhong Hu^{a,b}, Yongyong Tang^a, Qing Lan^a, Jiafei Xiao^a, Yan Tao^a, Mingliang Huang^{a,b}, Jiantang Peng^a, Leiluo Xu^a

^a State Key Laboratory of Ore Deposit Geochemistry, Institute of Geochemistry, Chinese Academy of Sciences, Guiyang 550081, China

^b University of Chinese Academy of Sciences, Beijing 100049, China

ARTICLE INFO

Keywords:

Trace elements
Sulfur isotope
Lanuoma Pb-Zn-Sb deposit
Sanjiang Tethys region

ABSTRACT

The Lanuoma deposit, located in the Sanjiang Tethyan metallogenic domain, shows a characteristic assemblage of Pb-Zn-Sb mineralization, distinguished from those in other sediment-hosted base metal deposits of this region. The ore textures reveal two mineralization stages: the early stage is characterized by Zn mineralization with occurrences of porous pyrite (Py2) and yellowish-brown sphalerites (Sp1), and the late stage is characterized by Sb-Pb mineralization with occurrences of subhedral-euhedral pyrite (Py3), yellowish-white sphalerites (Sp2), sulfosalts consisting of boulangerite, zinkenite, sorbyite and plagiogonite and calcite veins. The framboidal pyrites (Py1) predate Pb-Zn-Sb mineralization. Py2 has higher Zn contents (16.97–621.67 ppm, mean: 181.17 ppm) than Py3 (Zn: 0.76–323.44 ppm, mean: 29.58 ppm) by up to one order of magnitude. The Se contents of Py2 (Se: 5.46–87.82 ppm, mean: 50.96 ppm) are also one order of magnitude higher than those of Py3 (Se: 1.64–10.99 ppm, mean: 4.35 ppm). Sp1 is characterized by one order of magnitude higher contents of Fe (381.99–9046.64, mean: 4875.50 ppm) and Se (4.02–72.51 ppm, mean: 34.70 ppm) than Sp2 (Fe: 287.53–584.02 ppm, mean: 416.75 ppm; Se: 2.89–10.80 ppm, mean: 6.20 ppm). However, the average content of Cd (4256.38 ppm) in Sp2 is almost twice that in Sp1 (2635.74 ppm). The higher Se contents in Py2 coupled with higher Se and Fe contents in Sp1 indicate that Py2 and Sp1 had higher precipitation temperatures than Py3 and Sp2. Sulfur isotope compositions of pyrites and sphalerites acquired by NANO-SIMS and LA-MC-ICP-MS suggest two origins: the sulfur of Py2 ($\delta^{34}\text{S}$: -3.0 to 2.3%), Sp1 ($\delta^{34}\text{S}$: 0.2 – 0.9%) and Sp2 ($\delta^{34}\text{S}$: 0.7 – 2.5%) was mainly of magmatic source, and sulfur reduced via thermochemical sulfate reduction participated in the formation of Py3 ($\delta^{34}\text{S}$: 0.2 – 6.0%) and S-Sb-Pb minerals intergrown with Py3. The sulfur isotope compositions of Py1 ($\delta^{34}\text{S}$: -31.8 to -19.4%) indicate a biogenic origin associated with bacterial sulfate reduction. A fluid mixing model is suggested to interpret the genesis of the Lanuoma Pb-Zn-Sb deposit: mixing of a reduced S-bearing fluid with a metalliferous basinal brine resulted in the precipitation of sulfides. Temperature was the most important factor controlling metal precipitation in the Lanuoma deposit.

1. Introduction

In the Tethyan metallogenic domain, there are many well-known large lead–zinc deposits, such as the Reocin deposit, which has reserves of ~62 Mt of ore with grades of 8.7% Zn and 1.0% Pb (Velasco et al., 2003; Symons et al., 2009) and the Jinding deposit, which contains ~12.16 Mt of Zn and ~2.58 Mt of Pb (Xue et al., 2007). The Sanjiang region, which experienced diverse tectonic evolution and metallogeny, is an important part of the eastern Tethyan metallogenic domain and is drained by three major rivers: the Jinshajiang, Lancangjiang and

Nujiang (Deng et al., 2014a,b). Many diverse sediment-hosted metal deposits formed during the Cenozoic in response to its complicated tectonism and magmatism (Deng et al., 2014b; Wang et al., 2016; Fig. 1): for example, the world-class Jinding Zn-Pb deposit (Fu and Pang, 2004; Xue et al., 2007; Tang et al., 2014, 2017; Yalikhun et al., 2018), the Pb-Zn-Ag-Cu deposits in the Baiyangping area (He et al., 2005; Feng et al., 2011, 2014; Wang et al., 2011, 2015) and the Lalongla Pb-Zn deposit (Liu et al., 2013, 2017).

The element packages of mineralization in most of those deposits are Pb-Zn or Ag-Cu-Pb-Zn (e.g., the Jinding deposit, the Lalongla

* Corresponding author.

E-mail address: bixianwu@vip.gyig.ac.cn (X. Bi).

<https://doi.org/10.1016/j.oregeorev.2019.102941>

Received 22 October 2018; Received in revised form 7 May 2019; Accepted 20 May 2019

Available online 22 May 2019

0169-1368/ © 2019 Elsevier B.V. All rights reserved.

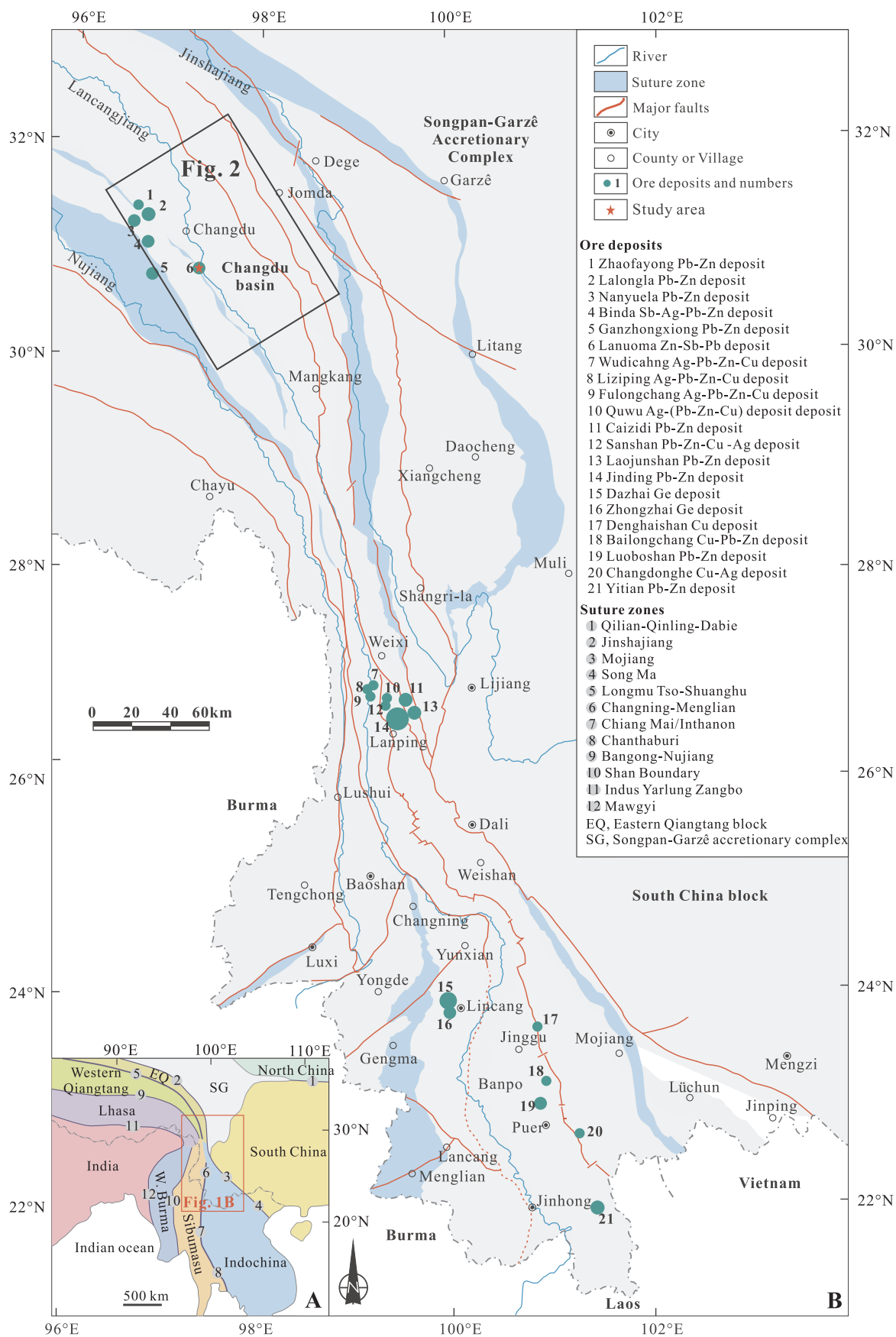


Fig. 1. Distribution of the Cenozoic sediment-hosted base metal deposits in the Sanjiang region (modified after Deng et al., 2014b).

deposit and the Baiyangping area) (Fig. 1). However, the Lanuoma deposit is characterized by the package Pb-Zn-Sb (Feng et al., 2006; Tao et al., 2011). This special metal association may indicate that the genesis of the Lanuoma deposit was different from those of other sediment-hosted base metal deposits in the region. Studies on the mineralization processes and sources of the Lanuoma Pb-Zn-Sb deposits would greatly enrich our understanding of the genesis and deposit type of base metal mineralization in the Sanjiang metallogenic belt. Nevertheless, the Lanuoma deposit has rarely received attention. Previous studies considered the metals and sulfur to be deeply sourced (Tao et al., 2011), in contrast to the perspective of crustal sources (e.g., basin basement) supported by mercury isotope evidence (Xu et al., 2018). Because previous studies generally adopted bulk analysis that may reflect average results of various generations of sulfides and therefore might not provide insights into significant information of the deposit origin, in situ analysis is necessary and important to understand the mineralization sources and processes.

Trace element compositions of pyrites and sphalerites play important roles in providing metallogenic information, and the method has been employed in numerous studies on different types of ore deposits (Gu and McClay, 1992; Large et al., 2007; Cook et al., 2009; Large et al., 2009; Maslennikov et al., 2009; Koglin et al., 2010; Ulrich et al., 2011; Ye et al., 2011; Reich et al., 2013; Agangi et al., 2013; Guy et al., 2014; Gregory et al., 2015; Genna and Gaboury, 2015; Gadd et al., 2016; Basori et al., 2018). Compared to conventional bulk analysis, sulfur isotope compositions of sulfides acquired by in situ techniques with high spatial resolution are more sensitive for reconstructing the temporal evolution of ore-forming fluids (Chen et al., 2017; Yan et al., 2018; Li et al., 2018). In this paper, we conduct careful research on the in situ compositions of trace elements and sulfur isotopes of texturally and paragenetically complex pyrites and sphalerites from the Lanuoma deposit by field emission scanning electron microscopy (FESEM), electroprobe microanalyzer (EPMA), laser ablation inductively coupled plasma mass spectrometry (LA-ICP-MS), laser ablation multicollector inductively coupled plasma mass spectrometry (LA-MC-ICP-MS) and nano secondary ion mass spectrometry (NANO-SIMS). This article discusses the sources of sulfur and presents a genetic model.

2. Geological setting

The Sanjiang Tethys has experienced the evolution of the Proto-Tethys, the Paleo-Tethys, the Meso-Tethys and the Neo-Tethys Oceans (Deng et al., 2014a). During the Cenozoic, the evolution was divided into four main phases (Deng et al., 2014b): (a) subduction and rollback of the Neo-Tethyan oceanic plate (before 45–40 Ma), (b) breakoff of the Neo-Tethyan slab (45–40 Ma) and diachronous removal of the lower lithospheric mantle (42–32 Ma), (c) underthrusting of the South China plate (32–10 Ma) and (d) subduction of the Indian oceanic plate (10 Ma to present). The Changdu basin, located in the northern part of the Sanjiang region, is bounded by the Leiwuqi-Zuogong microplate to the west and the Jomda-Weixi continental arc to the east (Tao et al., 2011). Mesozoic and Cenozoic intrusions are widespread in the Changdu area (Fig. 2). Indosinian magmatism occurred in southern Changdu and the Eocene magmatism is mainly exposed in northern Changdu (Fig. 2). The Jitang pluton (219.1 ± 1.7 Ma) is located in the Proterozoic Jitang group, approximately 3 km west of the Lanuoma deposit (Tao et al., 2014; Fig. 2). It is mainly composed of granodiorite and biotite granite (Tao et al., 2014). The Eocene felsic rocks in the northern part of the Changdu area are mainly located around Yulong (Hou et al., 2003; Guo et al., 2006; Jiang et al., 2006). The basement rocks mainly comprise metamorphic rocks (Jitang group, AnD jt) and granites (Feng et al., 2006). The basin is widely filled with Mesozoic sediments: Triassic sandstones, limestones, mudstones and shales and Jurassic sandstones and mudstones (Tao et al., 2011). Extensive tectonism and magmatism occurred in the basin in response to the collision of the Indian and Asian continents in the Cenozoic (Peng et al., 1997; Li et al., 2009). The

resultant faulting structures localized ore emplacement in the Triassic strata (Hou and Cook, 2009 and Tang et al., 2006).

The Lanuoma Pb-Zn-Sb deposit, approximately 10 km north of Jitang Town, is situated in the southeastern Changdu basin in the Sanjiang Tethyan metallogenic domain. The geological settings of the Lanuoma deposit have been documented by Feng et al. (2006) and Tao et al. (2011). The major strata exposed in the Lanuoma deposit include the upper section of the upper Triassic Jipila Formation, the upper Triassic Bolila Formation, the upper Triassic Adula Formation, the upper Triassic Duogaila Formation and the Quaternary sediments (Fig. 3). The upper section of the Jipila Formation consists of purplish red lithic sandstones and feldspathic quartz sandstones. The Bolila Formation is composed of clastic limestones and microcrystalline limestones. The Adula Formation comprises silty muds and shales interbedded with feldspathic quartz sandstones. The Duogaila Formation consists of two sections: the lower section consists of gray black silty muds and shales and carbonaceous muds/shales; the upper section consists of light gray lithic graywacke and feldspathic graywacke. There is massive upper Triassic gypsum in southwestern part of the ore district, and the gypsum is separated from the alteration zone by F1 (Fig. 3). The reverse faults that control the distribution of ore bodies are F1 and F2, and these faults are displaced by the transcurrent fault F3 (Fig. 3).

A stratiform orebody (No. I) and a vein orebody (No. II) are the main types of mineralization in the Lanuoma deposit (Feng et al., 2006). Both orebodies are hosted in the limestones of the Bolila Formation and controlled by F1 and F2 (Fig. 3). The average grades of Pb and Zn in the No. I orebody are 1.90 wt% and 3.04 wt%, respectively; the average grades of Pb and Zn in the No. II orebody are 1.86 wt% and 1.08 wt%, respectively (Feng et al., 2006). Major ore minerals include sphalerite, sulfosalt (S-Sb-Pb minerals), pyrite, orpiment, realgar and lesser amounts of galena (Fig. 4), and these minerals generally occur in the presence of calcite, gypsum, barite and quartz (Feng et al., 2006). Orpiment and realgar veins are distributed in the limestones (Fig. 4). The stratiform gypsum, located in south of the mine area and separated from the alteration zone by F1 (Fig. 3), is an evaporative origin. The barite generally occurs with gypsum in the fracture zone (Feng et al., 2006). The quartz occurs as anhedral or irregularly granular crystals or as aggregations in the calcite (Feng et al., 2006; Tao et al., 2011) and is related to the Pb-Sb mineralization (Tao et al., 2011). The calcitization and pyritization are related to the mineralization of Pb-Zn-Sb (Fig. 4). The calcite veins crosscut the sphalerites and intergrown with S-Sb-Pb minerals (Fig. 5).

3. Mineral morphology

In the Lanuoma deposit, three generations of pyrite have been identified. Pre-ore framboidal pyrite (Py1) exists in the form of spherical aggregates of pyrite microcrystals (less than 3 μ m in size) in limestone, which are generally considered a result of bacterial activity during syndeformation and syndiagenesis (Fig. 5A, Raiswell and Plant, 1980; Wilkin et al., 1996; Schieber, 2002; Folk, 2005; Large et al., 2007). Porous pyrite (Py2), rimmed by hydrothermal subhedral-euhedral pyrite (Py3), is intergrown with early stage sphalerite (Sp1) (Fig. 5B1, B2). Py3 is additionally characterized by oscillatory zoning (Fig. 5B2, C2) and is paragenetic with Sb-Pb sulfosalts and calcite (Fig. 5B1, B2, C1, C2, F). Sphalerite has been recognized into two stages: the early stage is expressed as yellow-brown sphalerite (Sp1), whereas the late stage is yellow-white sphalerite (Sp2) (Fig. 5D1, E1). Sp1 is clean without inclusions of sulfosalts inside crystals and generally occurs with a rim of Sp2 (Fig. 5D2, E2). Abundant sulfosalts are observed to occur in the pores and interstices of Sp2 grains (Fig. 5E2), suggesting that they were likely formed simultaneously. These sulfosalts consist of boulangierite, zinkenite, sorbyite and pligionite (Fig. 5F, H, G; for discussion, see 6.3.2). However, distinguishing these sulfosalts from one other is almost impossible due to the lack of distinct phase

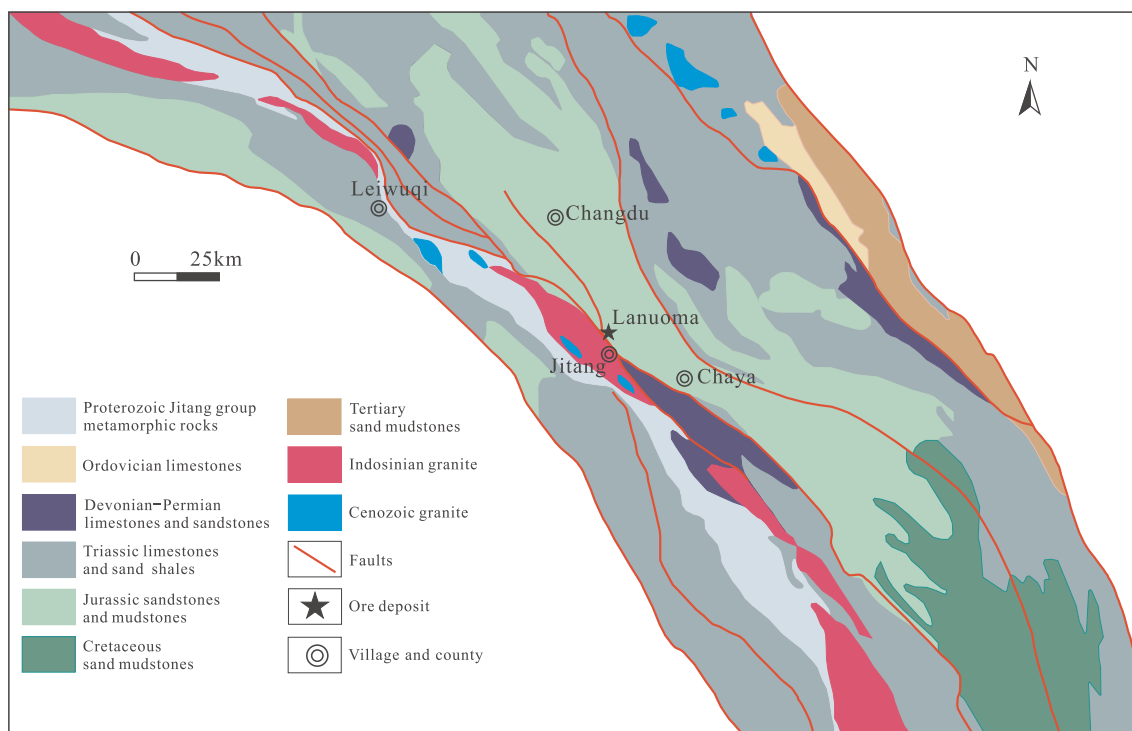


Fig. 2. Simplified regional geological map of the Changdu area (modified after Tao et al., 2011).

boundaries (Fig. 5F).

Based on the ore textures, crosscutting and paragenetic relationships, the formation of the deposit would have been achieved by the following steps (Fig. 6): i) pre-ore syndimentation and syndiagenesis, exemplified by framboidal Py1, no sphalerites and sulfosalts are observed from this period. ii) early-stage hydrothermal mineralization expressed as zinc-dominated mineralization (Sp1) in association with Py2; the sulfides are dominated by sphalerites (Sp1) followed by Py2. iii) late-stage hydrothermal mineralization characterized by Pb-Sb dominated mineralization accompanied by Sp2, Py3 and calcite; the major sulfides of this stage are the S-Sb-Pb minerals and Py3 and the Sp2 are the minority.

4. Samples and methods

A set of ore specimens was collected from ore heaps, and gypsum was collected from an outcrop in the Lanuoma mining district. An optical microscope and a JEOL JSM7800F FESEM were used to examine pyrite and sphalerite morphologies, mineral textures and assemblages on polished sections. The FESEM analysis was conducted under the conditions of 20 KeV, 10 nA and a beam size with a diameter of 1 μm at the State Key Laboratory of Ore Deposit Geochemistry, Institute of Geochemistry, Chinese Academy of Sciences (SKLODG, IGCAS). An EPMA was used to detect the contents of major elements in sulfosalts. Trace elemental and sulfur isotope compositions of different types of pyrites (Py1, Py2 and Py3) and sphalerites (Sp1 and Sp2) were examined by LA-ICP-MS, LA-MC-ICP-MS and NANO-SIMS.

4.1. EPMA

A JEOL JXA-8230 EPMA was used to evaluate the contents of As, Fe, Co, Ni, Zn, S, Pb, Se, Sb, Ge, Ga, Cd, and Mn in sulfosalts using a beam size with a diameter of 1 μm and a beam current of 20nA accelerated at 25 KeV at the Testing Center of Shandong Bureau of China Metallurgy and Geology. The detection limits of As, Se, Ge, Ga, Fe, Co, Ni, Zn, Mn, S, Pb, Cd and Sb were variable due to the effects of the beam current and acquisition times: 100 ppm for S, As, Se, Ga, Ge and Cd; 200 ppm

for Fe, Co, Ni, Mn and Sb; and 300 ppm for Zn and Pb. The following were used as standards: skutterudite for As and Co, pyrite for Fe and S, pentlandite for Ni, sphalerite for Zn, galena for Pb, bismuth selenide for Se, stibnite for Sb, germanium for Ge, gallium arsenide for Ga, cadmium for Ga, and rhodonite for Mn.

4.2. LA-ICP-MS

The contents of trace elements in pyrites and sphalerites were measured by LA-ICP-MS using an Agilent 7700x quadrupole mass spectrometer equipped with a GeolasPro 193 nm ArF excimer laser at the SKLODG, IGCAS. An energy density of 3.5–4.5 J cm^{-2} and a repetition rate of 7 Hz were used with laser spots 24 to 44 μm in diameter for samples, pure pyrite (an in-house standard), GSE-1, GSD-1 and MASS-1. An atmosphere of pure He (635 ml/min) was maintained during the whole ablation. The aerosols of samples and standards carried by pure He passed through a pulse-homogenizing device and then mixed with make-up gas of argon (900 ml/min) via a Y-connector before entering the torch.

To correct for mass bias and instrument drift, a standard-sample bracketing approach was used: the standards were analyzed twice before and after each group samples, and each group of samples consisted of 15 spots. The analysis process for each spot lasted 120 s, consisting of 15–20 s for background measurement (laser off), 60 s for signal collection (laser on) and 40–45 s to eliminate the memory effects (laser off). An in-house standard pyrite was used for calibration of the concentrations of S and Fe. The integrated count data of concentrations for other elements were calibrated and converted by GSE-1G and GSD-1G. The preferred values of element concentrations for the USGS reference glasses were from the GeoReM database (<http://georem.mpch-mainz.gwdg.de/>). The sulfide reference material MASS-1 was analyzed as an unknown sample to check the analytical accuracy. Data reduction was undertaken according to laser ablation data reduction software (LADR, <http://norris.org.au/ladr/>). Iron was used as the internal standard for quantification of pyrite, and Zn was used as the internal standard for quantification of sphalerite.

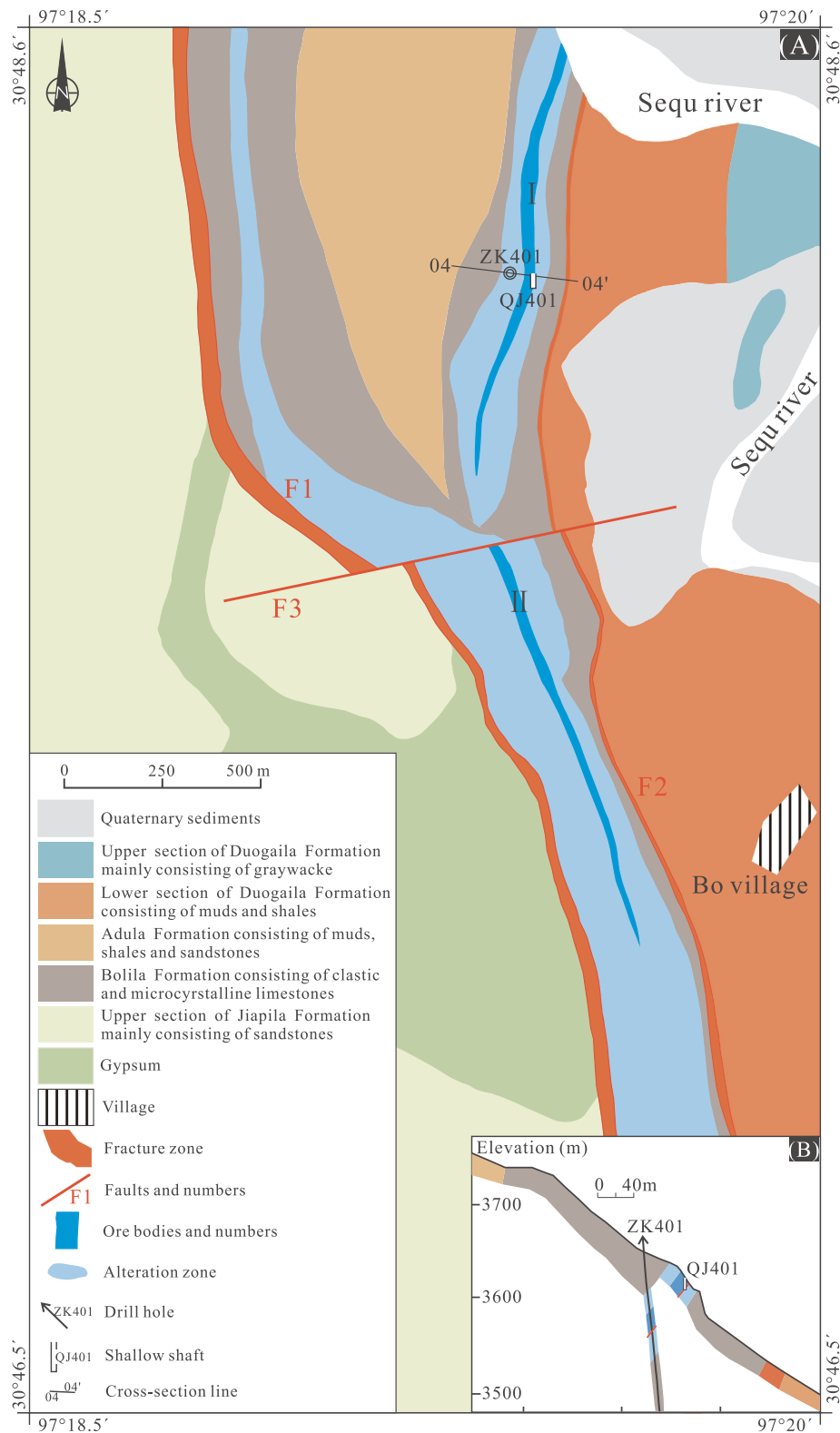


Fig. 3. (A) Geologic map of the Lanuoma deposit (modified after Feng et al., 2006). (B) Profile map of the cross-section line 04–04′ in the Lanuoma deposit (modified after Feng et al., 2006; Tao et al., 2011).

4.3. LA-MC-ICP-MS

Sulfur isotope measurements of sphalerite were accomplished by a high-resolution Nu Plasma 1700 MC-ICP-MS combined with a Resonics M50-LR excimer ArF laser ablation system (193 nm) at the State Key Laboratory of Continental Dynamics, Northwest University,

Xi'an, China. An energy density of 3.5–4 J/cm² and a repetition rate of 3–4 Hz were used with laser spots 37 μm in diameter for samples NBS123 and PSPT3. The standard-sample bracketing approach and repeated measurements of the calibrated standards (NBS123 and PSPT3) before and after each sample were used to correct for instrument drift and mass bias during the sulfur isotope analyses. Each scan

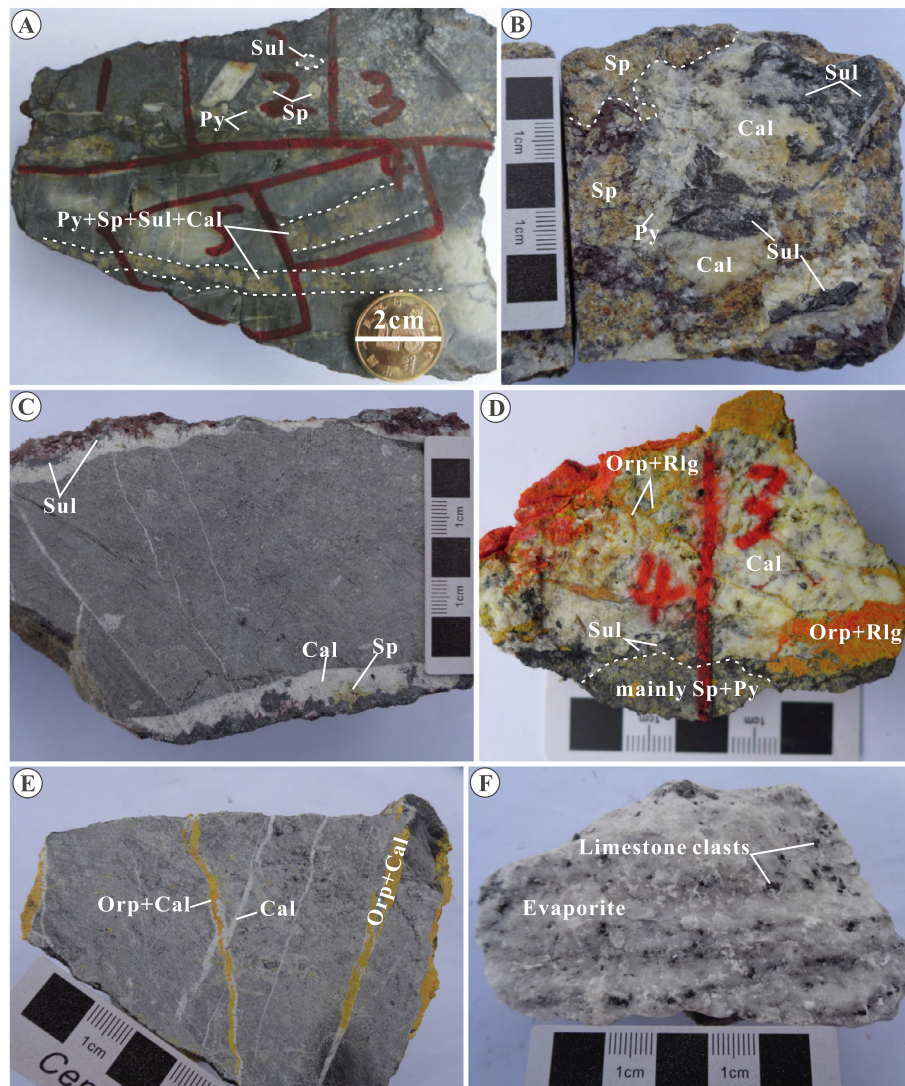


Fig. 4. Hand specimens from the Lanuoma Pb-Zn-Sb deposit. (A) Pyrites, sphalerites and sulfosalts are hosted in limestone as veins and fragments; (B, C) Pyrites, sphalerites and sulfosalts in calcite vein; (D) Orpiment, realgar and calcite crosscut the sulfides and sulfosalts; (E) Orpiment and realgar coexist with calcite; (F) Limestone clasts in evaporates. Abbreviations: Py-Pyrite; Sp-Sphalerite; Sul-Sulfosalts; Orp-Orpiment; Rlg-Realgar; Cal-Calcite.

comprised 50 s of ablation for signal collection and 60 s for background measurement (30 s before and after each signal collection). The procedural details for sulfur isotope measurements can be found in the references of [Chen et al. \(2017\)](#) and [Bao et al. \(2017\)](#).

4.4. NANO-SIMS

In situ sulfur isotope measurements and trace element mapping of pyrite were conducted on a CAMECA NanoSIMS 50L instrument at the Institute of Geology and Geophysics, Chinese Academy of Sciences, Beijing. The samples and working reference samples (pyrite PY-1117) were coated with carbon. Then, each area of $25 \times 25 \mu\text{m}^2$ was first presputtered with a primary beam of 100 pA for 2–3 min to remove the coating. Each presputtered area was acquired as ion images ($20 \times 20 \mu\text{m}^2$), and an interesting region was selected for measurement. The beam spot used in sulfur isotope measurements was $2 \times 2 \mu\text{m}^2$ for both samples and PY-1117 with the Faraday cup-electron multiplier (FC-EM-EM) detector mode (^{32}S with the FC, ^{34}S and other elements with the EM). Each sulfur isotope analysis lasted 150 s and consisted of 300 cycles of 0.5 s. The secondary electrons for $^{64}\text{Zn}^{32}\text{S}$, $^{75}\text{As}^{32}\text{S}$, $^{121}\text{Sb}^{32}\text{S}$ and $^{208}\text{Pb}^{32}\text{S}$ were used for the elemental mapping

(size: $50 \times 50 \mu\text{m}^2$). The procedural details for sulfur isotope measurements with NANO-SIMS can be found in [Zhang et al. \(2014\)](#) and [Yan et al. \(2018\)](#).

4.5. Sulfur isotope measurement of gypsum

Powdered samples of gypsum finer than 200 mesh were collected from the Lanuoma deposit and prepared for sulfur isotope measurement by a MAT-253 mass spectrometer using the conventional combustion method at the SKLOGD, IGCAS.

5. Results

5.1. Major element compositions of S-Sb-Pb minerals

The compositions of sulfosalts in the Lanuoma deposit are divided into four groups ([Table 1](#)). In Group 1 (boulangerite $\text{Pb}_5\text{Sb}_4\text{S}_{11}$); for discussion, see 6.3.2), the contents of S, Sb and Pb range from 18.41 to 19.16 wt%, 24.39 to 25.54 wt% and 55.81 to 56.82 wt%, respectively ([Table 1](#)). In Group 2 (zinkenite $\text{Pb}_6\text{Sb}_4\text{S}_{27}$); for discussion, see 6.3.2), the contents of S, Sb and Pb range from 22.89 to 23.33 wt%, 39.23 to

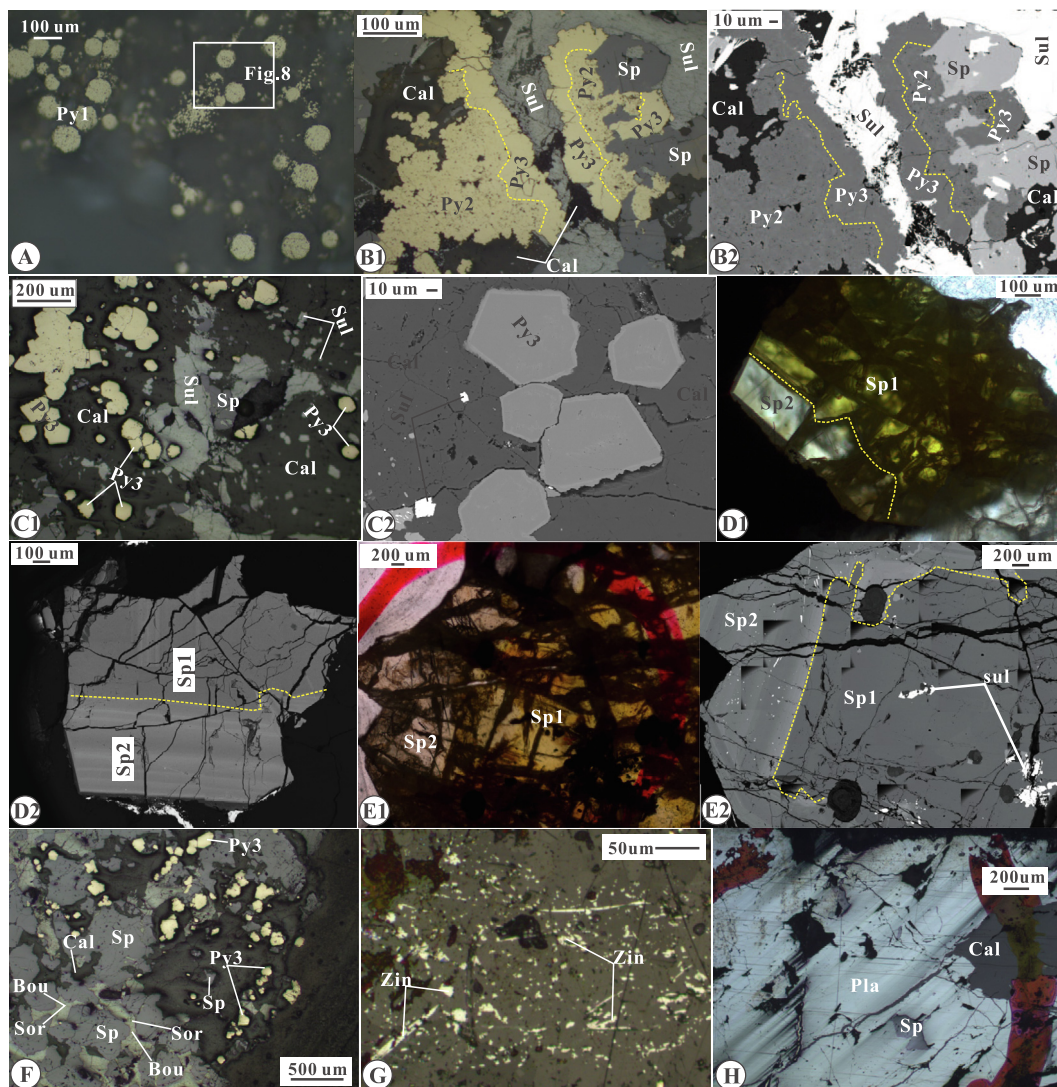


Fig. 5. Reflected-light photomicrographs and backscattered electron images (B2, C2, D2 and E2) of different types of pyrite, sphalerite and sulfosalt morphology from the Lanuoma Pb-Zn-Sb deposit. (A) Framboidal pyrites (Py1); (B1, B2) Porous pyrites (Py2) overgrown by subhedral pyrite (Py3) and sulfosalts crosscut Py2 and Py3; (C1, C2) Euhedral pyrites (Py3); (D1, D2, E1, E2) Yellowish-brown sphalerites (Sp1) surrounded by yellowish-white sphalerites (Sp2); (F) No distinct phase boundaries between boulangerite and sorbyite; (G) Zinkenite microvein in limestone; (H) Plagionite encircling sphalerite. Abbreviations: Py-Pyrite; Sp-Sphalerite; Sul-Sulfosalts; Cal-Calcite; Bou-Boulangerite; Sor-Sorbyite; Zin-Zinkenite; Pla-Plagionite.

40.55 wt% and 31.89 to 32.36 wt%, respectively (Table 1). In Group 3 (sorbyite ($Pb_{17}(Sb,As)_2S_{50}$); for discussion, see 6.3.2), the contents of S, Sb and Pb range from 20.35 to 20.85 wt%, 34.23 to 34.81 wt% and 44.27 to 46.89 wt%, respectively (Table 1). In Group 4 (plagionite ($Pb_5Sb_8S_{17}$); for discussion, see Section 6.3.2), the contents of S, Sb and Pb range from 20.83 to 21.40 wt%, 35.66 to 38.12 wt% and 38.80 to 40.62 wt%, respectively (Table 1).

5.2. Trace element characteristics of pyrites

To eliminate disturbances from mineral microinclusions, trace elements, which are generally present as solid solutions in pyrites and sphalerites, were selected, and the analysis spots were localized in the areas of pyrites and sphalerites free from microinclusions. The Co, Ni, Se, As, Cu, Ag, Tl, Sb and Pb of the pyrites were used to reconstruct the history of hydrothermal evolution. Only smooth segments of the time-resolution profile curve of LA-ICP-MS were chosen to calculate the concentrations of the selected trace elements (Fig. 7). Because the grains of Py1 are too small to locate the beam spots precisely (Fig. 5), the metallogenic elements (Pb-Zn-Sb) in Py1 were mapped by NANO-

SIMS. The results show that lead-antimony minerals are present only as intergranular filling of framboidal pyrites (Fig. 8).

5.2.1. Co and Ni

For Py2, the nickel contents (0.59–22.80 ppm) and average value (5.63 ppm) are higher than the cobalt contents (0.02–1.48 ppm) and average value (0.30 ppm) by up to one or two orders of magnitude, respectively (Table 2 and Fig. 9). Most of the analyses of Py3 have very low concentrations of Co and Ni, below the detection limits (Table 2), but the average value of Ni (1.87 ppm) is also one order of magnitude higher than that of Co (0.14 ppm) (Fig. 9).

5.2.2. Zn, Se, Tl, Ag, As, Sb, Pb and Cu

Zn, Se and Tl are significantly enriched in Py2 and range from 16.97 to 621.67 ppm, 5.46 to 87.82 ppm and 0.68 to 26.52 ppm, respectively (Table 2 and Fig. 9). The Zn, Se and Tl contents of Py3 range from 0.76 to 323.44 ppm, 1.64 to 10.99 ppm and 0.03 to 4.16 ppm, respectively (Table 2 and Fig. 9). The average contents of Zn (181.17 ppm), Se (50.96 ppm) and Tl (12.05 ppm) in Py2 are one or two orders of magnitude higher than those of Zn (29.58 ppm), Se (4.35 ppm) and Tl

Minerals	Pre-ore	Mineralization stage		Post-ore
		Early	Late	
Py1	————			
Py2		————		
Py3			————	
Sp1		————		
Sp2			————	
Sul			————	
Calcite			————	————
Quartz			————	
Orp/Rlg			————	
Gypsum	————			
Barite	————			

Fig. 6. Relative growth sequence of main minerals and mineralization stage division in the Lanuoma deposit. Abbreviations: Py-Pyrite; Sp-Sphalerite; Sul-Sulfosalts consisting of Boulangerite, Sorbyite, Zinkenite and Plagionite; Orp-Orpiment; Rlg-Realgar.

(0.75 ppm) in Py3 (Table 2 and Fig. 9). The content distributions of Ag, As, Sb and Pb in Py2 range from 29.43 to 94.79 ppm, 6427.17 to 28515.15 ppm, 1684.76 to 9183.85 ppm and 1908.03 to 7080.67 ppm, respectively (Table 2 and Fig. 9). The contents of Ag, As, Sb and Pb in Py3 range from 0.87 to 53.04 ppm, 1277.88 to 26359.78 ppm, 35.98–7380.73 ppm and 46.86–5202.61 ppm, respectively (Table 2 and Fig. 9). The average values of Ag, As, Sb and Pb in Py2 are 57.37 ppm, 13808.32 ppm, 4163.29 ppm and 4031.27 ppm, respectively (Table 2 and Fig. 9). Py3 has lower average values of Ag, As, Sb and Pb, which are 21.70 ppm, 9355.57 ppm, 1524.03 ppm and 1658.9 ppm,

Table 1

EPMA data (in wt%) of sulfosalts from the Lanuoma Pb-Zn-Sb deposit and the atomic ratios of S:Pb:Sb.

Spots	As	Fe	Co	Ni	Zn	S	Pb	Se	Sb	Ge	Ga	Cd	Mn	Total	S:	Pb:	Sb
Boulangerite																	
LN12-1@2-2	0.20	0.06	0.02	bdl	nd	18.69	56.82	nd	25.23	nd	nd	0.14	0.03	101.19	2.8	1.3	1
LN12-1@2-3	0.20	0.04	0.04	nd	nd	18.55	56.64	nd	25.17	0.01	nd	0.09	nd	100.74	2.8	1.3	1
LN12-1@2-4	0.22	0.02	0.06	0.02	nd	18.59	55.93	nd	25.11	nd	0.01	0.07	0.05	100.08	2.8	1.3	1
LN12-1@2-5	0.22	nd	0.03	nd	nd	18.96	56.56	nd	25.54	0.04	nd	0.19	0.08	101.61	2.8	1.3	1
LN12-1@2-6	0.20	0.08	nd	nd	0.42	19.16	56.02	nd	25.50	0.06	0.02	0.06	0.06	101.57	2.9	1.3	1
LN12-1@2-7	0.12	nd	nd	0.03	nd	18.72	56.05	nd	24.96	0.06	0.02	0.15	bdl	100.12	2.9	1.3	1
LN12-1@2-8	0.37	0.38	nd	nd	nd	18.41	55.81	nd	24.39	0.01	nd	0.03	nd	99.41	2.9	1.3	1
Zinkenite																	
LN5-5@7-1-11e	3.33	nd	nd	nd	nd	23.03	31.96	nd	40.55	nd	0.01	0.12	nd	99	4.9	1	2.2
LN5-5@7-1-13e	4.45	nd	bdl	bdl	nd	23.24	32.2	nd	39.42	nd	0.04	0.02	nd	99.38	5	1	2.1
LN5-5@7-1-14e	4.04	0.02	nd	nd	nd	23.33	31.91	nd	39.57	0.04	0.02	0.07	nd	99	5.1	1	2.1
LN5-5@7-1-15e	4.19	0.02	bdl	nd	nd	23.04	32.05	nd	39.23	nd	0.01	0.04	nd	98.59	5	1	2.1
LN5-5@7-2-5e	4.21	nd	nd	nd	nd	23.18	32.17	0.01	40.18	nd	nd	0.07	0.03	99.84	5	1	2.1
LN5-5@7-2-6e	3.4	bdl	nd	nd	bdl	23.03	31.89	0.02	40.01	nd	nd	0.08	0.02	98.47	5	1	2.1
LN5-5@7-2-7e	2.88	nd	bdl	0.04	nd	22.89	32.01	0.02	40.55	0.06	nd	0.1	bdl	98.56	4.9	1	2.2
LN5-5@7-2-8e	3.3	bdl	nd	0.05	nd	22.94	32.36	nd	40.1	0.04	0.01	0.1	0.04	98.95	4.9	1	2.1
Sorbyite																	
LN12-1@2-1e	0.2	nd	nd	nd	nd	20.63	44.69	nd	34.23	nd	nd	0.08	nd	99.83	3	1	1.3
LN12-1@2-15e	0.26	0.23	bdl	0.03	0.79	20.85	44.48	0.05	34.81	nd	nd	0.13	0.08	101.72	3	1	1.3
LN12-1@2-16e	0.15	nd	nd	nd	2.2	20.35	44.27	nd	34.29	0.01	0.02	0.05	0.04	101.37	3	1	1.3
Plagionite																	
17LN11-1@2-4e	0.54	bdl	nd	nd	nd	21.4	39.77	nd	37.85	nd	0.04	0.03	bdl	99.66	3.5	1	1.6
17LN11-1@2-5e	0.51	0.06	0.07	nd	bdl	21.23	40.28	nd	37.79	0.02	0.03	0.06	nd	100.07	3.4	1	1.6
17LN11-2@2-7e	0.46	0.05	0.03	nd	nd	21.02	39.92	nd	36.99	nd	0.01	0.11	0.01	98.6	3.4	1	1.6
17LN11-2@2-8e	0.39	bdl	nd	nd	0.06	21.17	40.62	0.05	37.57	nd	nd	0.05	0.03	99.96	3.4	1	1.6
17LN11-2@3-2e	0.38	0.02	nd	nd	nd	21.04	38.8	nd	38.12	0.03	nd	0.05	nd	98.44	3.5	1	1.7
17LN11-2@4-1e	0.57	bdl	0.02	nd	nd	20.83	40.53	0.19	36.87	nd	nd	0.03	bdl	99.05	3.3	1	1.6
17LN11-1@3-1e	1.41	bdl	nd	0.04	0.06	22.92	40.62	nd	35.66	0.04	nd	0.15	nd	100.91	3.7	1	1.5

nd-not detected

bdl-below the detection limit

respectively (Table 2 and Fig. 9). However, Py3 has a wider distribution range of copper contents (29.98 to 601.24 ppm) than Py2 (51.14 to 468.67 ppm). The average Cu value of Py3 (265.75 ppm) is also higher than that of Py2 (167.52 ppm) (Table 2 and Fig. 9).

5.3. Trace element characteristics of sphalerites

5.3.1. Se, Mn and Fe

This group of elements is characterized by enrichment in Sp1, and the contents of Se, Mn and Fe range from 4.02 to 72.51 ppm, 0.46 to 16.55 ppm and 381.99 to 9046.64 ppm, respectively (Table 3 and Fig. 10). The distributions of Se (2.89–10.80 ppm), Mn (0.49–1.15 ppm) and Fe (287.53–584.02 ppm) in Sp2 are more concentrated (Table 3 and Fig. 10). The average contents of Se (34.70 ppm), Mn (9.58 ppm) and Fe (4875.50 ppm) in Sp1 are higher than those of Se (6.20 ppm), Mn (0.79 ppm) and Fe (416.71 ppm) in Sp2 by up to one order of magnitude.

5.3.2. Cd

This element is characterized by enrichment in Sp2, and the Cd contents of Sp1 are significantly lower than those of Sp2 (Table 3, Fig. 10). The Cd contents of Sp2 range from 2964.36 ppm to 5011.48 ppm (Table 3 and Fig. 10). The Cd content of Sp1 ranges from 1285.69 ppm to 4111.76 (Table 3 and Fig. 10). The average content of Cd (4256.38 ppm) in Sp2 is twice as high as that of Cd (2635.74 ppm) in Sp1.

5.4. Sulfur isotope systematics

The sulfur isotope compositions of gypsum and different types of pyrites and sphalerites are presented in Table 4. The $\delta^{34}\text{S}$ values of gypsum are 15.5‰, 15.6‰, 15.6‰ and 15.6‰ (Table 4 and Fig. 11). The $\delta^{34}\text{S}$ values of Py1 range from -31.8 to -19.4 ‰ with an average value of -25.8 ‰ (Table 4 and Fig. 11). The $\delta^{34}\text{S}$ values of Py2 range

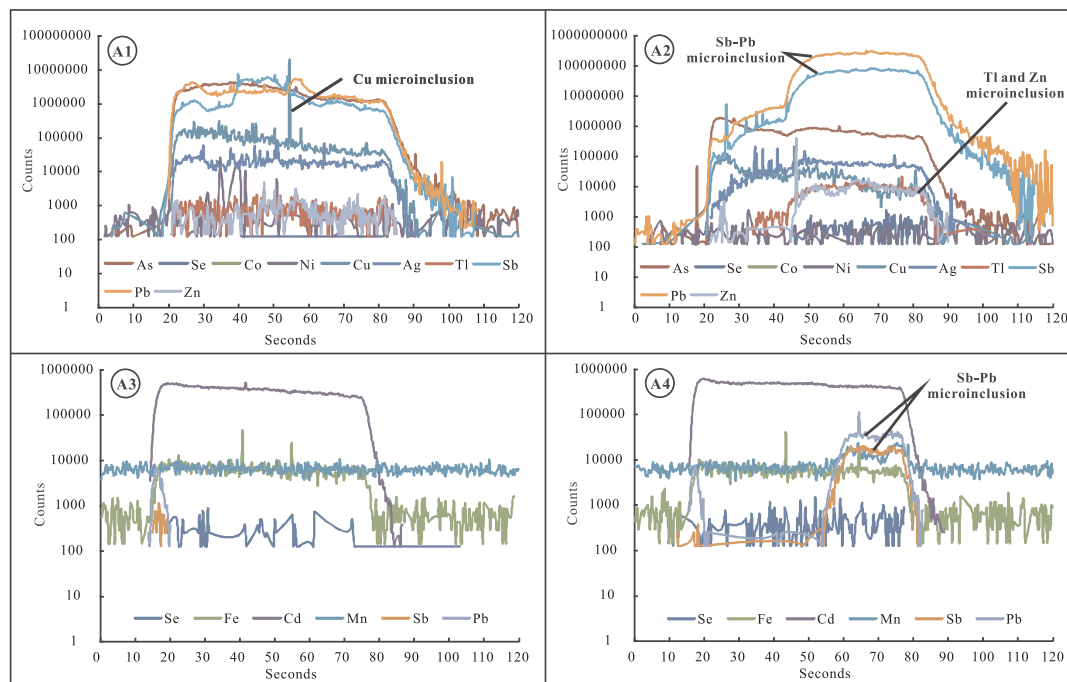


Fig. 7. Representative time-resolved depth profiles for pyrites (A1, A2) and sphalerite (A3, A4) suggest that Zn-Cd microinclusions are present in pyrites and Sb-Pb microinclusions are presented in sphalerites.

from -3.0 to $+2.3\text{‰}$ with an average value of -0.1‰ (Table 4 and Fig. 11). The distribution range of $\delta^{34}\text{S}$ values ($\delta^{34}\text{S}$: $+0.2$ to $+6.0\text{‰}$) in Py3 is significantly wider than that in Py2 (Fig. 11). The sulfur isotope compositions between Sp1 and Sp2 have a tiny but significant variation: except for the value of 0.7‰ , all of the other $\delta^{34}\text{S}$ values ($\delta^{34}\text{S}$: $+1.0$ to $+2.5\text{‰}$) of Sp2 are greater than 1.0‰ ; however, all of the $\delta^{34}\text{S}$ values ($\delta^{34}\text{S}$: $+0.2$ to $+0.9\text{‰}$) of Sp1 are less than 1.0‰ (Table 4 and Fig. 11).

6. Discussion

6.1. Control of temperature on metal precipitation

Maslennikov et al. (2009) and Genna and Gaboury (2015) documented that pyrites formed at higher temperatures with higher Se contents due to the substitution between Se and S. The up to one order of magnitude higher Se contents in Py2 than in Py3 imply a higher precipitation temperature (Fig. 9). Se, Fe, Cd and Mn are present in sphalerite crystal lattices (Fig. 7A3, A4). Sphalerites that form at high temperature (e.g., skarn-type Pb-Zn deposits) are enriched in Fe, and sphalerites formed under medium–low temperatures (e.g., MVT type Pb-Zn deposits) are characterized by high contents of Cd (Ye et al., 2011; Cook et al., 2009; Wen et al., 2016). The higher Se and Fe contents and lower Cd contents of Sp1 imply that the formation temperature of Sp1 was higher than that of Sp2 (Fig. 10). In addition, the homogenization temperatures of the fluid inclusions in sphalerites range from 153 °C to 250 °C (Xu, 2017), and the fluid inclusions in calcites intergrowth with S-Sb-Pb minerals have the lower homogenization temperatures ($140\text{ °C} - 220\text{ °C}$) (Tao et al., 2011). The decreasing homogenization temperatures of the fluid inclusions from the early Zn mineralization to the late Pb-Sb mineralization are consistent with the decreasing contents of Fe and Se from the Sp1 to Sp2 (Fig. 10). In conclusion, the growth sequence of minerals in the Lanuoma deposit and their chemical compositions suggest that temperature decreased from early Zn mineralization to late Pb-Sb mineralization and controlled metal precipitation. As a consequence, the metals contents (e.g., the Co, Ni, Zn, Ag, Sb, Tl and Pb) significantly decreased from the Py2

to the Py3 (Fig. 9).

6.2. Sulfur origin

Ohmoto and Rye (1979) documented that several potential sulfur sources including mantle sulfur, marine sulfate and biogenic sulfur may possibly be involved in hydrothermal ore deposits. The sulfur isotope compositions ($\delta^{34}\text{S}_{\text{CDT}}$) of the mantle are heterogeneous but cluster around 0‰ (Thode et al., 1961; Chaussidon et al., 1989; Torssander, 1989; Eldridge et al., 1995; Seal et al., 2000; Seal, 2006). The sulfur isotope compositions of Permian and Triassic marine sulfates range from 10 to 20‰ (Seal et al. 2000; Canfield and Farquhar, 2009). Generally, sulfates in geological settings produce H_2S through two mechanisms: bacterial sulfate reduction (BSR) and TSR. Because the survival temperature of sulfate-reducing bacteria is below 110 °C (usually less than 60 °C to 80 °C), BSR occurs below the temperature of 110 °C (Jørgensen et al., 1992; Canfield, 2001; Machel, 2001). However, TSR needs higher temperatures, generally greater than 80 °C to 100 °C (Machel et al., 1995; Machel, 2001). Several factors, including pressure, temperature, oxygen fugacity and pH of hydrothermal fluids and sulfur isotope compositions, can affect sulfur isotope fractionation (Ohmoto, 1972; O'Neil, 1986). At upper crust conditions, the effect of pressure is minimal (Seal, 2006). Because the mineral association in the Lanuoma deposit shows there is no sulfate coprecipitated with pyrites, sphalerites and sulfosalts, the $\delta^{34}\text{S}$ values of sulfides are approximately equal to the $\Sigma\delta^{34}\text{S}$ value of the ore-forming fluid. Because pyrites with no intergrown sulfates occurred through the mineralization progress, the effects of pH and f_{O_2} on sulfur isotopic fractionation were limited (Ohmoto, 1972). The fractionation between sulfides and the solution from which the sulfides precipitated is insignificant when the temperature is below 350 °C (e.g., the relative isotopic enrichment factor for pyrite are generally less than 0.8‰ between 150 and 250 °C ; Ohmoto, 1972). Because homogenization temperatures of fluid inclusions in sphalerites from the Lanuoma deposit range from 153 °C to 250 °C (Xu, 2017), the effect of temperature would have been insignificant. Excluding the pressure and the temperature, f_{O_2} and pH of the hydrothermal fluid, the sulfur isotope compositions (sulfur origins) are

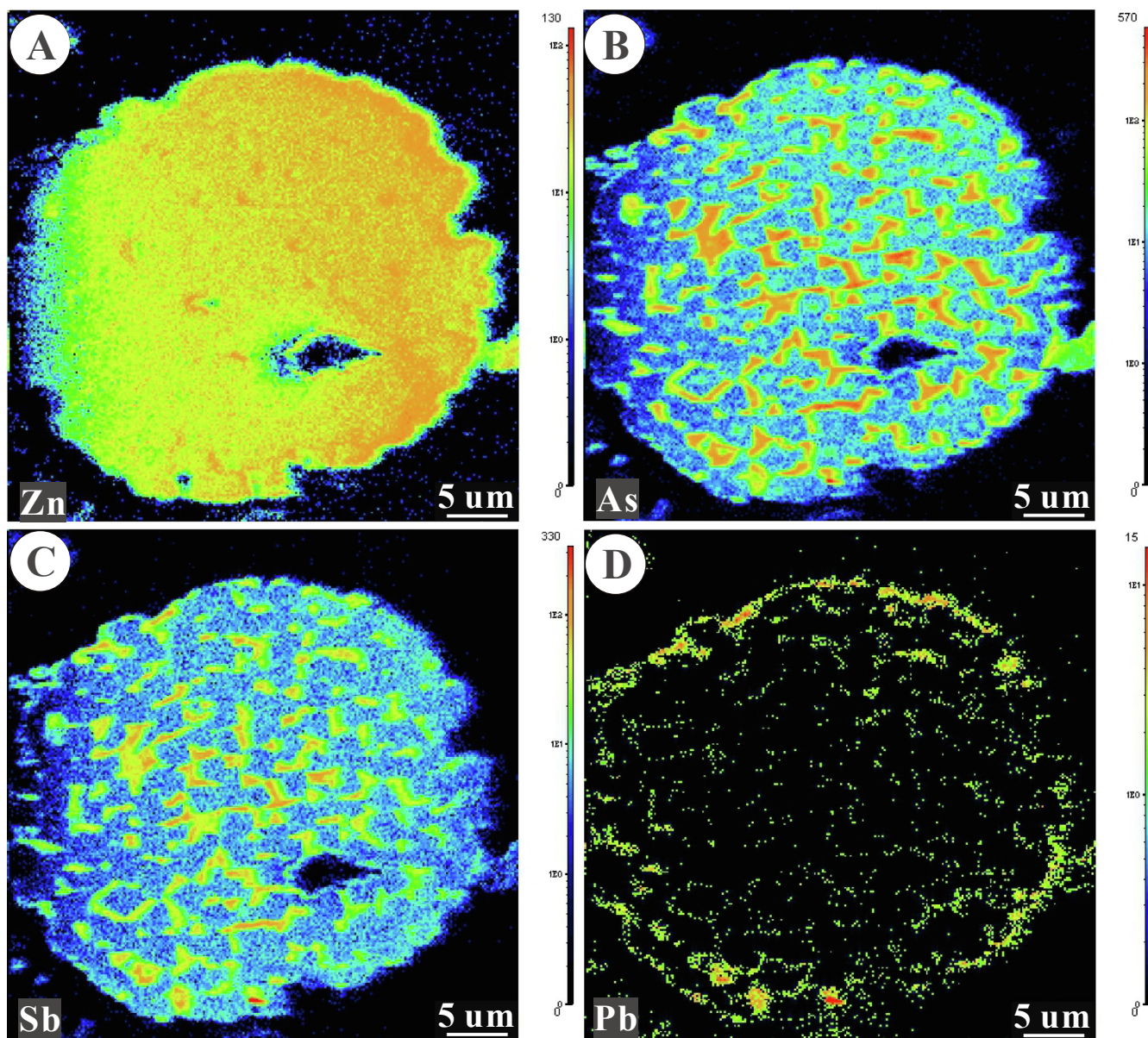


Fig. 8. NANO-SIMS mapping analysis of (A) Zn, (B) As, (C) Sb and (D) Pb of framboidal pyrites from the Lanuoma Pb-Zn-Sb deposit. Note that the color scales of these images indicate relative signal intensities, not absolute contents.

important potential factors that affect the composition of sulfur isotopes in the Lanuoma deposit.

Biogenic sulfur is characterized by large variations with dominantly negative $\delta^{34}\text{S}$ values. Canfield and Teske (1996) suggested that fractionations between SO_4^{2-} and H_2S in association with BSR range from 24 to 71‰. The sulfur isotope fractionations between gypsum (average $\delta^{34}\text{S}$ value: 15.5‰) and Py1 ($\delta^{34}\text{S}$ values: -31.8 to -19.4 ‰) are up to 47.3‰, which are typical sulfur isotope compositions produced by BSR. The $\delta^{34}\text{S}$ values of Py2 (-3.0 to 2.3‰), Sp1 (0.2 to 0.9‰) and Sp2 (0.7 to 2.5‰) remain consistent with the values reported by Tao et al. (2011), likely indicating magmatic sourced sulfur. In comparison, Py3 shows relatively heavier sulfur isotope compositions ($\delta^{34}\text{S}$: 0.2 to 6.0‰) that are obviously distinguished from those of Py1, Py2, Sp1 and Sp2 (Table 4 and Fig. 11). This indicates an addition of sulfur from sedimentary sources. The average $\delta^{34}\text{S}$ value (15.5‰) of the gypsum in the Lanuoma deposit (Fig. 3) falls within the range of $\delta^{34}\text{S}$ for Triassic marine sulfates (Seal et al., 2000; Canfield and Farquhar, 2009), which supports an evaporative origin for this gypsum. The S-Sb-Pb minerals and pyrites associated with the residual gypsum (Fig. 12) indicate that

the gypsum contributed to the formation of Py3. Therefore, sulfate reduction was most likely involved in the formation of Py3. Homogenization temperatures of fluid inclusions in sphalerites from the Lanuoma deposit range from 153 °C to 250 °C (Xu 2017), under which sulfate-reducing bacteria are unable to survive, but the temperatures are beneficial for TSR. In addition to high temperature, TSR requires sulfates (SO_4^{2-}) and reductants (Machel et al., 1995; Machel, 2001). The gypsum in the mine could be a favorable source of SO_4^{2-} . Tao et al. (2011) documented that the ore-forming fluid was characterized by hydrocarbon-bearing basin brine that may provide required reductants. Although TSR is a complex multistage process (Ma et al., 2008; Meshoulam et al., 2016), sulfur fractionations between SO_4^{2-} and H_2S caused by TSR range from 0 to 20‰ (Machel et al., 1995; Meshoulam et al., 2016). Accordingly, the $\delta^{34}\text{S}$ values of Py3 (0.2 to 6.0‰) fall within the range of $\delta^{34}\text{S}$ values produced by TSR. Moreover, the $\delta^{13}\text{C}_{\text{PDB}}$ (-4.9 to $+3.0$ ‰) and Sr isotope compositions ($^{87}\text{Sr}/^{86}\text{Sr}$: 0.7080–0.7085) of calcite related to the Pb-Sb mineralization suggest that the carbon and strontium were mainly from shallow carbonates (Tao et al., 2011; Xu, 2017). Based on these evidences, the sulfate-

Table 2
Trace element contents (in ppm) of different types of pyrites from the Lanuoma Pb-Zn-Sb deposit.

Spots	Co	Ni	Cu	Zn	As	Se	Ag	Sb	Tl	Pb
Porous pyrite (Py2)										
LNMI2-1@1-31a	0.05*	0.79*	63.66	27.65	8953.45	61.34	50.35	2840.31	13.21	3060.95
LNMI2-1@1-33a	0.58	12.24	118.59	34.82	17210.38	84.01	47.26	4043.25	25.46	3390.57
LNMI2-1@1-38la	0.14	4.44	53.21	170.14	7604.17	78.07	35.38	2117.64	20.89	4259.31
LNMI2-1@1-39la	0.14	2.08	230.97	621.67	18738.16	42.97	44.61	4873.29	8.44	2967.93
LNMI2-1@1-40la	0.04	0.59	385.71	255.14	18598.38	12.92	56.83	2540.41	2.6	3304.72
LNMI2-1@1-41la	0.42	0.77	170.24	564.17	6427.17	5.46	45.24	2879.45	0.68	3427.46
LNMI2-1@1-42la	0.03*	4.59	232.52	97.02	15632.7	28.64	77.97	3972.14	8.59	4073.85
LNMI2-1@1-44la	0.11	1.02	51.14	137.84	7312.98	68.42	29.43	2845.87	9	1908.03
LNMI2-1@1-45la	0.04	0.6	76.74	433.63	7558.06	62.08	39.17	1684.76	16.68	1908.84
LNMI2-1@1-46la	1.18	3.74	124.01	83.61	12348.84	64.57	69.95	4717.12	17.74	4980.45
LNMI2-1@1-48la	0.04	11.22	246.18	42.09	13395.58	34.93	82.4	5311.53	4.62	6265.47
LNMI2-1@1-49la	0.14	1.95	85.5	428.36	11733	70.78	54.7	3603.84	14.35	3508.67
LNMI2-1@1-50la	0.16	4.28	205.72	109.95	11689.58	43.05	94.79	5227.58	9.19	5243.74
LNMI2-1@1-53la	0.06	2.44	159.74	21.77	15481.4	42.89	41.17	9183.85	6.39	7080.67
LNMI2-1@1-54la	0.43	11.21	159	26.6	13446.91	64.48	59.82	5113.56	16.94	4726.95
LNMI2-1@1-56la	0.18	9.18	336.35	589.09	23246.73	17.74	85.42	3574.13	4.03	3057.17
LNMI2-1@1-58la	0.06	2.76	468.67	63.46	28515.15	15.48	79.76	4940.67	3.7	5687.95
LNMI2-1@1-70la	0.02*	0.62	70.35	16.97	9474.17	78.82	53.04	4693.81	19.86	4366.21
LNMI2-1@1-71la	0.42	20.17	74.9	25.85	12272.35	87.82	49.53	4767.29	17.02	4031.84
LNMI2-1@1-72la	1.48	22.8	73.47	29.89	14196.88	66.88	49.97	4777.6	26.52	3862.33
LNMI2-1@1-73la	0.68	0.81	131.22	24.95	16138.65	38.78	57.92	3720.91	7.19	3543.48
Subhedral to anhedral pyrite (Py3)										
LNMI2-1@1-11a	0.15	0.44*	483.72	3.52	21652.63	3.88	28.64	1614.32	0.46	2135.31
LNMI2-1@1-2la	0.03*	0.71*	333.19	1.01	4812.7	2.52	1.245	55.49	0.03*	71.18
LNMI2-1@1-3la	0.04	0.49*	189.17	3.52	6616.9	1.91	31.65	1765.87	0.44	2012.48
LNMI2-1@1-5la	0.03*	0.51*	93.08	1.32	3674.39	2	9.315	441.94	0.13	568.88
LNMI2-1@1-6la	0.04*	0.63*	221.03	0.76	4019.73	2.39	9.075	611.83	0.15	762.46
LNMI2-1@1-7la	0.03*	0.44*	313.16	15.24	10332.26	3.78	36.37	2790.39	0.68	2794.79
LNMI2-1@1-8la	0.03	0.52*	421.9	5.68	14320.83	3.63	35.71	2532.4	0.8	3061.39
LNMI2-1@1-9la	0.04*	0.55*	29.98	3.22	1288.17	2.99	39.25	2178.81	0.33	2686.41
LNMI2-1@1-10la	0.04*	0.69*	30.95	1.8	1277.88	3.05	7.875	407.28	0.16	493.75
LNMI2-1@1-11la	0.04*	0.67*	57.75	14.71	2080.29	2.15	2.99	177.25	0.06	209.3
LNMI2-1@1-12la	0.04*	0.65*	57.62	0.91	2456.81	1.94	2.235	124.38	0.04	128.06
LNMI2-1@1-13la	0.04*	0.51*	327.88	8.35	7798.31	3.47	15.51	1056.54	0.39	1002.96
LNMI2-1@1-14la	0.04*	0.63*	40.38	2.76	1699.41	2.31	4.015	124.98	0.12	148.94
LNMI2-1@1-15la	0.03*	0.53*	72.29	1.12	3281.36	2.28	0.87	35.98	0.03	46.86
LNMI2-1@1-16la	0.06	1.15	379.2	6.32	17180.48	6.72	35.33	1647.3	1.03	1964.33
LNMI2-1@1-17la	0.03*	0.75*	271.11	16.26	12730.73	4.65	21.47	1439.54	0.51	1032.11
LNMI2-1@1-18la	0.93	0.67*	422.72	37.5	17474.24	3.59	35.62	3061.79	1.08	2765.56
LNMI2-1@1-19la	0.1	0.68*	360.26	23.74	10806.68	3.01	53.04	4175.3	2.37	5202.61
LNMI2-1@1-20la	0.12	1.84*	521.22	7.52	19991.98	5.26	40.77	7380.73	0.98	3200.98
LNMI2-1@1-21la	0.03*	0.61*	393.99	18.65	15220.73	7.38	42.78	3354.55	0.94	3831.47
LNMI2-1@1-22la	0.04*	0.76*	89.69	22.5	1649.71	3.73	9.465	305.84	0.3	458.4
LNMI2-1@1-24la	0.48	0.66*	330.37	13.53	16440.51	6.06	16.23	916.15	0.29	1034.3
LNMI2-1@1-26la	0.54	0.60*	174.61	10.96	7792.59	3.07	15.93	611.23	0.53	644.3
LNMI2-1@1-27la	0.03*	0.57*	215.67	3.11	7826.44	4.55	6.785	298.35	0.18	428.16
LNMI2-1@1-28la	1.05	0.71	286.69	1.31	16136.89	6.21	8.055	456.91	0.2	574.16
LNMI2-1@1-29la	0.04*	0.63*	77.39	2.38	3482.62	2.13	14.15	811.25	0.2	1113.02
LNMI2-1@1-63la	0.07	0.67*	343.91	18.47	6916.56	1.64	28.38	1686.63	0.43	2086.07
LNMI2-1@1-67la	0.03*	0.56*	437.22	10.74	9806.78	2.92	33.57	2309.13	0.52	2684.1
LNMI2-1@3-11a	0.05	16.94	601.24	2.03	21020.9	4.64	27.72	2714.5	0.85	3553.75
LNMI2-1@3-2la	0.02*	2.4	464.83	1.95	14018.66	3.38	17.68	1865.76	0.33	2422.97
LNMI2-1@3-3la	0.07	1.22	525.77	1.4	15224.49	5.6	17.05	1666.8	0.39	2164.28
LNMI2-1@3-5la	0.03*	0.38*	572.84	7.4	23984.79	8.04	32.73	1628.89	1.98	2195.06
LNMI2-1@3-6la	0.05*	0.66*	582.42	23.49	26359.78	8.62	22.28	2037.59	0.79	2659.59
LNMI2-1@3-7la	0.67	0.73*	138.02	30.38	3333.23	2.3	11.19	538.08	0.35	609.21
LNMI2-1@3-8la	0.04*	0.7*	58.29	6.12	1495	2.28	18.89	1029.89	0.35	1338.57
LNMI2-1@3-9la	0.05*	0.73*	82.96	1.69	1733.74	2.47	10.49	547.61	0.12	650.4
LNMI2-1@3-10la	0.07*	0.77*	109.64	0.87	1901.64	2.5	12.26	725.78	0.19	855.72
LNMI2-6@1-11a	0.69	11.21	347.37	15.42	10399.45	5.78	17.09	1249.43	0.69	1307.67
LNMI2-6@1-2la	0.14	1.35	242.55	45.45	6415.13	5.88	31.12	2378.4	1.15	2459.72
LNMI2-6@1-3la	0.13	1.6	453.66	323.44	24553.28	10.99	41.48	2085.64	2.4	2673.76
LNMI2-6@1-4la	0.02*	0.43*	178.93	4.87	5210.57	7.48	35.31	2000.54	0.54	2616.31
LNMI2-6@1-5la	0.04	12.66	234.68	18.96	9214.37	6.85	27.41	1359.09	0.71	1484.29
LNMI2-6@1-7la	0.12	5.48	386.02	1.75	7152.76	2.94	8.11	576.14	0.21	685.48
LNMI2-6@1-8la	0.04	1.58	359.3	188.26	12726.98	4.29	19.32	1790.25	2.92	1328.45
LNMI2-6@1-9la	0.1	11.19	193.51	297.06	9632.81	9.85	41.01	3007.18	4.16	3440.34
LNMI2-6@1-10la	0.04*	0.56*	143.46	11.72	4334.01	7.44	6.09	508.82	1.08	490.82
LNMI2-6@1-11la	0.03*	0.9	156.35	86.97	4695.1	5.26	17.19	1286.28	0.3	1654.34
LNMI2-6@3-11a	0.11	0.55*	137.43	117.23	4340.01	4.81	43.7	2469.25	3.64	2444.27
LNMI2-6@3-4la	0.03*	0.73*	76.2	6.1	1907.62	2.35	18.89	839.27	0.42	1073.99

* the detection limit was used to represent the content when concentrations were below detection limit

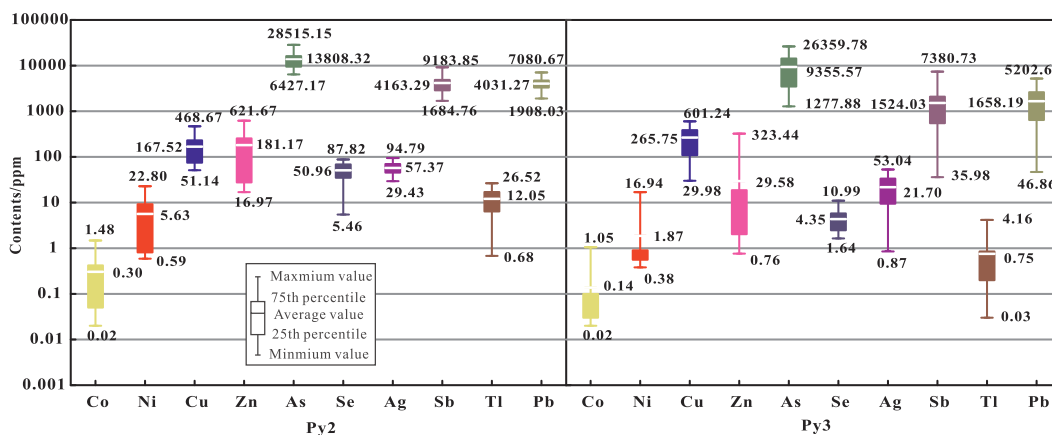


Fig. 9. Concentrations and distributions of trace elements acquired from Py2 and Py3 by LA-ICP-MS.

Table 3
Trace element contents (in ppm) of different types of sphalerites from the Lanuoma Pb-Zn-Sb deposit.

Spots	Mn	Fe	Se	Cd	Spots	Mn	Fe	Se	Cd
Sp1					Sp2				
17LNM1-6@1-3	6.39	5730.05	51.2	2822.55	17LNM1-6@1-1	0.64	412.81	6.73	4369.84
17LNM1-6@1-4	6.98	6379.16	56.32	2842.75	17LNM1-6@2-2	0.75	403.97	8.64	4847.81
17LNM1-6@1-5	7.98	5672.49	45.51	2888.71	17LNM1-6@2-3	0.64	519.47	5.63	3418.72
17LNM1-6@2-5	5.2	3408.88	18.71	1285.69	17LNM1-6@2-10	0.74*	584.02	10.8	5011.48
17LNM1-6@2-7	0.46	440.18	5.49	3031.14	17LNM1-6@2-11	0.85	426.62	6.74	4137.53
17LNM1-6@2-8	0.53	381.99	4.02	2874.87	17LNM1-6@2-12	1.02	456.34	7.3	4310.59
17LNM1-6@2-9	0.69	535.77	7.53	4111.76	17LNM1-6@2-13	0.88	422.75	4.93	4341.68
17LNM1-6@3-5	12.52	9046.64	72.51	2217.11	17LNM1-6@2-14	0.69	475.15	4.35	4432.95
17LNM1-6@3-6	8.13	5052.54	23.21	1903.17	17LNM1-6@3-2	0.59*	436.87	4.75	4315.68
17LNM1-6@3-7	16.55	5541.09	17.43	3023.14	17LNM1-6@3-4	0.83	487.01	6.36	4519.27
17LNM1-6@3-8	9.72	3478.38	9.77	2243	17LNM1-6@7-1	0.84	472.53	6.12	4597.49
17LNM1-6@7-5	10.81	6953.33	39.96	1901.01	17LNM1-6@7-2	0.56*	287.53	4.1	3667.65
17LNM1-6@7-6	14.05	5667.92	19.63	3010.22	17LNM1-6@7-3	0.58	352.85	2.89	3511.63
17LNM1-6@7-7	10.14	4979.07	32.87	2598.37	17LNM1-6@7-4	0.49	411.89	3.05	2964.36
17LNM1-3@1-6	12.91	5857.22	52.19	2631.47	17LNM1-3@1-1	0.84	341.41	5.46	4342.42
17LNM1-3@1-8	12.15	5311.21	39.27	2570.61	17LNM1-3@1-2	0.83*	367.29	5.31	4318
17LNM1-3@1-9	12.65	5823.22	62.13	2487.57	17LNM1-3@1-3	1.15	385.78	4.56	4151.08
17LNM1-3@3-4	14.74	5830.43	53.62	2670.24	17LNM1-3@1-4	0.83	379.83	5.51	4175.54
17LNM1-3@3-5	15.19	6111.55	50.39	2606.79	17LNM1-3@1-5	0.74	434.63	5.61	3836.57
17LNM1-3@3-6	13.73	5308.83	32.18	2994.7	17LNM1-3@3-1	1.02	364.76	8.11	4562.16
					17LNM1-3@3-2	0.88	356.6	9.51	4854.01
					17LNM1-3@3-3	1.09	387.57	9.88	4953.97

* the detection limit was used to represent the content when concentrations were below detection limit

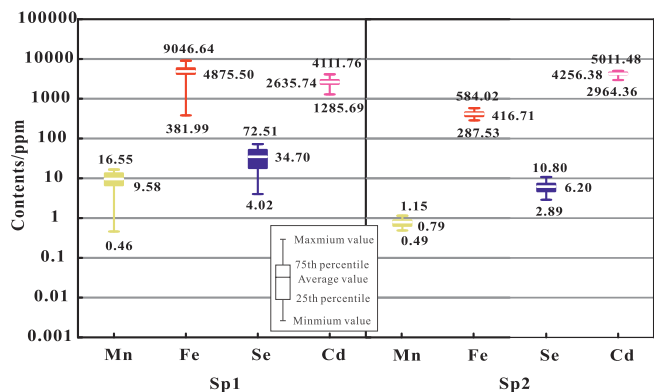


Fig. 10. Concentrations and distributions of trace elements acquired from Sp1 and Sp2 by LA-ICP-MS.

reduced sulfur via TSR is considered to have participated in the formation of Py3.

In conclusion, the sulfur isotope system of the Lanuoma deposit may imply two origins: magmatic source and sulfates. The sulfurs in Py2

were mainly of magmatic source. The sulfurs in Py1 were produced by BSR, and the sulfurs of Py3 were affected by TSR. Because Sp1 coexists with Py2, the sulfurs in Sp1 may also have been derived from the magmatic source. The sulfurs in Sp2 may have an origin similar to that of sulfurs in Py2 and Sp1 according to the comparable sulfur isotope compositions. The comparable sulfur isotope compositions between Sp2 and Py2 (and/or Sp1) would be explained by the $\delta^{34}\text{S}$ of Sp2 being inherited from magmatic sulfur but affected by the sulfate reduced sulfurs via TSR. The sulfurs produced via TSR probably also participated in the formation of S-Sb-Pb minerals based on the paragenesis between Py3 and S-Sb-Pb minerals.

6.3. Ore genesis of the Lanuoma Pb-Zn-Sb deposit

6.3.1. Transport of zinc, lead and antimony

Complexes of Cl^- , HS^- and OH^- are the most important ligands in hydrothermal fluids (Giordano, 2002; Kesle, 2005; Tagirov and Seward, 2010; Mei et al., 2015; Zhong et al., 2015). Numerous studies (Kesle, 2005; Yardley, 2005; Tagirov and Seward, 2010; Mei et al., 2015; Zhong et al., 2015 and references therein) have documented that lead and zinc are transported by chloride complexes in brine. Temperature, pressure, pH, salinity, redox state and the total sulfur of the fluid

Table 4
Sulfur isotopic compositions of gypsum and different types of pyrites and sphalerites from the Lanuoma Pb-Zn-Sb deposit.

Spots	$\delta^{34}\text{S}_{\text{v-CDT}}$	Spots	$\delta^{34}\text{S}_{\text{v-CDT}}$	Spots	$\delta^{34}\text{S}_{\text{v-CDT}}$	Spots	$\delta^{34}\text{S}_{\text{v-CDT}}$
Gypsum (Gy)		lnm12-1@1-4_mg_11	-1.2	lnm12-1@5-1_mg_4	5.1	17LNMI-6@4-2	0.6
Gy-1	15.5	lnm12-1@1-4_mg_12	-3.0	lnm12-1@5-1_mg_5	4.9	17LNMI-6@6-2	0.7
Gy-2	15.6	lnm12-1@1-8_mg_21	-0.4	lnm12-1@5-1_mg_6	5.1	17LNMI-6@7-5	0.5
Gy-3	15.6	lnm12-1@1-8_mg_22	-1.2	lnm12-1@5-1_mg_7	6.0	17LNMI-6@7-6	0.5
Gy-4	15.6	lnm12-1@1-9_mg_23	0.3	lnm12-1@5-1_mg_8	3.5	17LNMI-6@7-7	0.4
Framboidal pyrite (Py1)		lnm12-1@1-9_mg_24	2.3	lnm12-1@5-2_mg_1	1.2	Yellowish-white sphalerite (Sp2)	
lnm2-1@1-1_mg_1	-23.1	Subhedral to anhedral pyrite (Py3)		lnm12-1@5-2_mg_2	1.8	17LNMI-3@1-1	1.3
lnm2-1@1-1_mg_2	-23.9	lnm12-1@1-1_mg_3	2.9	lnm12-1@5-2_mg_3	1.2	17LNMI-3@1-2	1.4
lnm2-1@1-1_mg_3	-24.2	lnm12-1@1-1_mg_4	4.3	lnm12-1@5-2_mg_4	1.6	17LNMI-3@1-3	1.1
lnm2-1@1-1_mg_4	-25.7	lnm12-1@1-2_mg_5	1.6	lnm12-1@5-3_mg_1	3.5	17LNMI-3@2-1	1.2
lnm2-1@1-1_mg_5	-26.6	lnm12-1@1-2_mg_6	1.6	lnm12-1@5-3_mg_2	4.5	17LNMI-3@3-1	1.1
lnm2-1@1-1_mg_6	-24.7	lnm12-1@1-2_mg_7	2.0	lnm12-1@5-3_mg_3	2.0	17LNMI-3@3-2	0.7
lnm2-1@1-2_mg_1	-25.4	lnm12-1@1-3_mg_8	0.2	lnm12-1@5-3_mg_4	2.5	17LNMI-6@1-1	1.1
lnm2-1@1-2_mg_2	-26.6	lnm12-1@1-3_mg_9	1.9	lnm12-1@5-3_mg_5	3.0	17LNMI-6@1-2	2.0
lnm2-1@1-2_mg_3	-27.8	lnm12-1@1-3_mg_10	2.0	Yellowish-brown sphalerite (Sp1)		17LNMI-6@1-4	1.9
lnm2-1@1-2_mg_4	-19.4	lnm12-1@1-5_mg_13	1.8	17LNMI-3@1-4	0.9	17LNMI-6@2-1	1.1
lnm2-1@1-2_mg_5	-23.9	lnm12-1@1-5_mg_14	1.7	17LNMI-3@1-5	0.9	17LNMI-6@2-3	1.6
lnm2-1@1-2_mg_6	-25.7	lnm12-1@1-6_mg_15	1.1	17LNMI-3@1-6	0.8	17LNMI-6@3-1	1.2
lnm2-1@1-3_mg_1	-27.5	lnm12-1@1-6_mg_16	1.5	17LNMI-3@2-2	0.9	17LNMI-6@3-2	1.2
lnm2-1@1-3_mg_2	-27.0	lnm12-1@1-7_mg_17	1.8	17LNMI-3@3-3	0.8	17LNMI-6@3-3	2.3
lnm2-1@1-3_mg_3	-28.1	lnm12-1@1-7_mg_18	1.5	17LNMI-3@3-4	0.7	17LNMI-6@4-1	1.4
lnm2-1@1-3_mg_4	-31.8	lnm12-1@1-7_mg_19	2.1	17LNMI-6@1-3	0.5	17LNMI-6@6-1	1.3
lnm2-1@1-3_mg_5	-27.8	lnm12-1@1-7_mg_20	3.1	17LNMI-6@2-2	0.2	17LNMI-6@7-1	1.0
Porous pyrite (Py2)		lnm12-1@5-1_mg_1	3.1	17LNMI-6@2-4	0.6	17LNMI-6@7-2	2.0
lnm12-1@1-1_mg_1	0.2	lnm12-1@5-1_mg_2	3.1	17LNMI-6@3-4	0.6	17LNMI-6@7-3	2.5
lnm12-1@1-1_mg_2	1.9	lnm12-1@5-1_mg_3	3.9	17LNMI-6@3-5	0.2	17LNMI-6@7-4	2.2

control the solubility and precipitation of Zn and Pb (Cooke et al., 2000; Yardley, 2005). The transportation of Sb is more complex than those of Zn and Pb. Below 350 °C, Sb is transported as the species hydroxy-chlorides, hydroxy (Sb(OH)₃), bisulfide (HSb₂S⁴⁻), hydroxybisulfide (Sb₂S₂(OH)₂) and/or chlorides in chloride or chloride-free solution (Wood et al., 1987; Krupp, 1988; Williams-Jones and Normand, 1997; Pokrovski et al., 2006). Obolensky et al. (2007) documented that Sb is dissolved mainly as hydroxy-chloride complexes in acidic high-chloride moderate temperature (below 300 °C) solutions and as hydroxide (Sb(OH)₃) in low to moderate temperature (below 250–300 °C) weak-neutral high-chloride solutions. Soluble chloride-hydroxide complexes

of Sb are also possible but as a minor phase in acid to nearly neutral high-chloride solutions (Obolensky et al., 2007). The solubility of Sb is controlled by the contents of dissolved chlorine and sulfur, temperature, pH and oxidation–reduction state, of which the temperature and pH are the most important factors (Krupp, 1988; Pokrovski et al., 2006; Williams-Jones and Normand, 1997; Obolensky et al., 2007). Although we cannot determine the degree of acidity or alkalinity of the metalliferous hydrothermal fluid, the pH of the fluid was probably neutral because of the buffering action of the limestones that are widely distributed in the Changdu basin (Fig. 2). The bulk analyses of gases and liquids from fluid inclusions in calcites intergrown with S-Sb-Pb

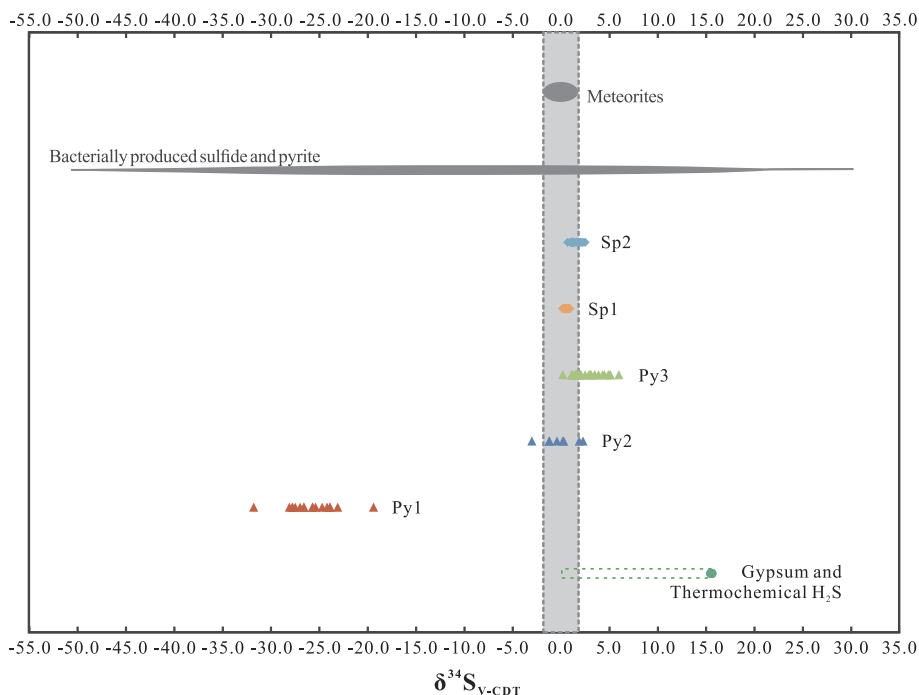


Fig. 11. Sulfur isotope composition of gypsum and different types of pyrites and sphalerites (modified after Seal et al., 2000; Warren, 1999).

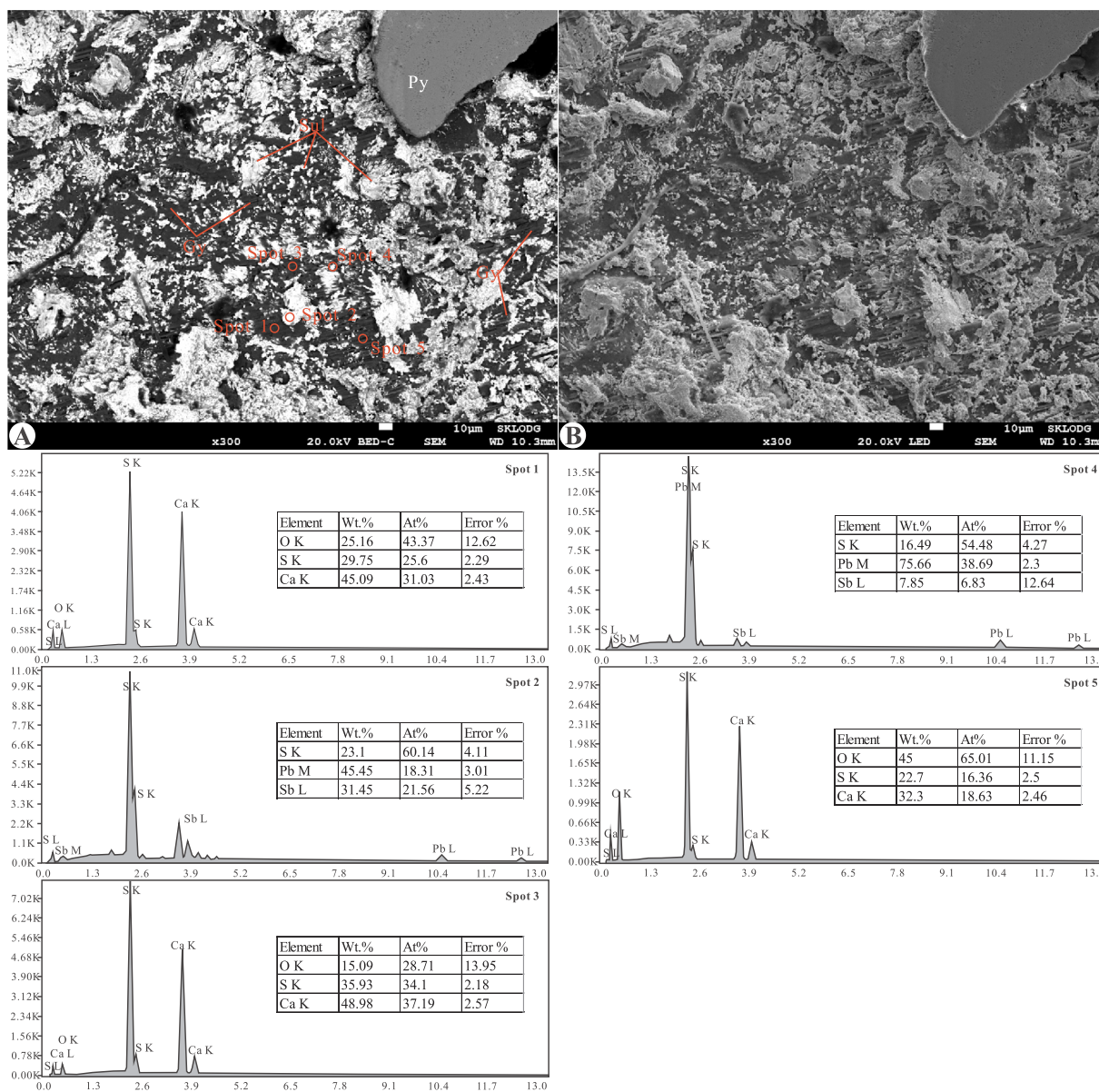


Fig. 12. (A) Sulfosalts associated with residual gypsum in a backscattered electron image; (B) Secondary electron image shows the fiber-like texture of gypsum. Abbreviations: Gy-Gypsum; Sul-Sulfosalts; Py-Pyrite.

minerals showed that the anions were dominated by chloridions and subsequently by fluorinions (Tao et al., 2011). The fluid inclusions in sphalerites from the Lanuoma deposit demonstrate that the homogenization temperatures range from 153 to 250 °C with an average of 189 °C and that salinities range from 3.87 to 19.05 wt% NaCl equiv with an average of 11.6 wt% NaCl equiv (Xu, 2017). Based on the previous discussion, the features of the metalliferous hydrothermal fluid were appropriate for the transport of Zn and Pb as chloride complexes and of Sb most likely as chloride-hydroxide complexes or hydroxides.

6.3.2. Precipitation process of the Lanuoma Pb-Zn-Sb deposit

The fluid mixing model, local sulfate reduction model and reduced sulfur model are generally used to account for precipitation processes of sediment-hosted base metal deposits. The reduced sulfur model requires base metals and reduced sulfur to be transported in the same fluid to the depositional site, and precipitation results from cooling, pH change, fluid dilution and devolatilization (Anderson, 1973, 1975; Sverjensky, 1981, 1986). To accomplish the coexistence between base metals and reduced sulfur, a low pH value (less than 4.5) and high temperature

(greater than 200 °C) are required (Anderson, 1975; Sverjensky, 1981; 1986; Cooke et al., 2000). Widespread carbonate rocks in the Lanuoma mining district may be unfavorable for this model due to the neutralization between H^+ and CO_3^{2-}/HCO_3^{-} . The local sulfate reduction model involves base metals and oxidized sulfur (SO_4^{2-}) transportation in the same fluid, and this fluid is brought to depositional sites where the oxidized sulfur is reduced to S^{2-} by reductants (e.g., methane, bitumen, oil, and gas) and sulfides therefore precipitate (Olson, 1984; Garven, 1985; Cooke et al., 2000). For this model, an evaporitic setting is not required, and acid is not generated when sulfides precipitate at the site where S^{2-} is generated (Anderson and Garven, 1987). A fluid mixing model means that H_2S -rich fluid encounters metal-rich but reduced sulfur-poor brine at the precipitation site (Anderson, 1973, 1975; Sverjensky, 1986; Anderson, 2008). Corbella et al. (2004) suggested that this mixing model is efficient and can be used to interpret carbonate dissolution, collapse features and carbonatization. The compositions of the fluid inclusions in the sphalerites and calcites indicate that the metallogenic fluid of the Lanuoma deposit was characterized by basinal brine (Tao et al., 2011; Xu, 2017). And Xu et al. (2018)

documented that the sulfide minerals shared the similar mercury isotope compositions with the metamorphic basement and the hydrothermal altered wall rocks and suggested that the metals (e.g., Hg, Pb and Zn) were probably mainly derived from the basement rocks of the Changdu basin. Because the metalliferous basinal brine and the reduced S-bearing fluid have different origins, the local sulfate reduction model is not suitable, but the fluid mixing model is appropriate for the genesis of the Lanuoma Pb-Zn-Sb deposit. In addition, the acid generated in the mixing model caused carbonate dissolution, collapse features and carbonization (Figs. 4 and 5).

Magmatism at depth provided the fluid containing sulfur and might have triggered the formation and transportation of brine-containing metals; then, these two fluids migrated upward along faults and fractures, and sulfides were deposited when the fluids mixed. Although the temperature, pH and other factors (such as the redox state of the fluid) control the precipitation of Zn, Pb and Sb (Williams-Jones and Normand, 1997; Cooke et al., 2000; Yardley, 2005; Pokrovski et al., 2006), the controls of the pH and the redox state of the fluid may have been weak due to the buffering of the widespread limestones and the lack of drastic change in the redox state of the metallogenetic fluid (no oxides intergrown with sulfides and sulfosalts, as discussed above). During mixing, a decrease in temperature may have been the most important factor that controlled the precipitation of metals, especially for Sb as the solubility of Sb decreases sharply when cooling to medium–low temperatures (Krupp, 1988; Williams-Jones and Normand, 1997; Pokrovski et al., 2006). According to Craig and Barton (1973), pyrite, boulangerite and zinkenite occur in sequence with decreasing temperature. This finding also suggests that cooling controlled the metal precipitation. The sharp decreases in the contents of Se and Fe from Py2 and Sp1 to Py3 and Sp2 also demonstrate that the temperature decreased significantly from the early (Zn) mineralization stage to the late (Pb-Sb) mineralization stage (as discussed in the Section 6.1). The involvement of TSR is a favorable factor causing a decrease in temperature because the formation water containing soluble gypsum (as SO_4^{2-}) joined the ore-forming fluids. As a result, the composition of $\delta^{13}\text{C}_{\text{V-PDB}}$ and $\delta^{18}\text{O}_{\text{V-SMOW}}$ of hydrothermal calcite related to Pb-Zn-Sb mineralization shows a mixed signal of deep fluids and shallow carbonates (Tao et al., 2011). Note that during the mixing of these two fluids, the magmatic sulfur was consumed to form sulfides, and TSR was activated; these processes resulted in the earlier sulfides (e.g., Py2, Sp1) having signals of magmatic sourced sulfur and the later sulfides (e.g., Py3) having sulfur isotope signals produced by TSR. Moreover, more sulfur is required to form sulfosalts than galena in the Lanuoma deposit. Calculation of sulfosalt chemical formulas shows that the ratios of S:Sb:Pb vary from 2.8 (or 2.9):1.3, 4.9 (or 5.0):2.1 (or 2.2):1, 3.0:1.3:1 and 3.4 (or 3.5):1.6:1, indicating the presence of sulfosalts: boulangerite ($\text{Pb}_5\text{Sb}_4\text{S}_{11}$), zinkenite ($\text{Pb}_6\text{Sb}_{14}\text{S}_{27}$), sorbyite ($\text{Pb}_{17}(\text{Sb},\text{As})_{22}\text{S}_{50}$) and pligionite ($\text{Pb}_5\text{Sb}_8\text{S}_{17}$). (Fig. 5H, G). The TSR process in the Lanuoma deposit ensured the supply of sulfur.

7. Conclusions

The hydrothermal evolution and mineralization processes of the Lanuoma Pb-Zn-Sb deposit are reconstructed based on pyrite morphologies, trace element compositions and sulfur isotope compositions of pyrite and sphalerite. Consequently, several conclusions are drawn as follows:

- (1) Two mineralization stages are identified: the early stage mainly involved Zn mineralization and is characterized by the mineral assemblage of Py2 and Sp1, and the late stage mainly involved Pb-Sb mineralization and is characterized by the mineral assemblage of Py3, Sp2, S-Sb-Pb minerals and calcite.
- (2) Magmatic sourced sulfur mainly contributed to the formation of Py2 and Sp1, and sulfur reduced via TSR may have participated in the formation of Py3, Sp2 and S-Sb-Pb minerals.

- (3) The fluid mixing model is an appropriate interpretation of the genesis of the Lanuoma deposit: magmatism at depth provided some of the sulfur and triggered the migration of metal-rich basinal brine, and sulfide and sulfosalts precipitated when these two fluids mixed.

Acknowledgements

This research is financially supported by the National Key Basic Research Program (2015CB452603), the CAS/SAFEA International Partnership Program for Creative Research Teams (KZZD-EW-TZ-20) and the National Natural Science Foundation (41703047). We thank the Senior Engineer Zhihui Dai, Yanwen Tang and Shaohua Dong for their assistance in the process of experiments. We also thank the editors and anonymous reviewers for their constructive suggestions and comments that are greatly helpful to an improvement of our paper.

Appendix A. Supplementary data

Supplementary data to this article can be found online at <https://doi.org/10.1016/j.oregeorev.2019.102941>.

References

- Agangi, A., Hofmann, A., Ueberwasser, C.C.W., 2013. Pyrite Zoning as a Record of Mineralization in the Ventersdorp Contact Reef, Witwatersrand Basin, South Africa. *Econ. Geol.* 108, 1243–1272.
- Anderson, G.M., 1973. The Hydrothermal Transport and Deposition of Galena and Sphalerite Near 100°C. *Econ. Geol.* 68, 480–492.
- Anderson, G.M., 1975. Precipitation of Mississippi Valley-Type Ores. *Econ. Geol.* 70, 937–942.
- Anderson, G.M., 2008. The Mixing Hypothesis and the Origin of Mississippi Valley-Type Ore Deposits. *Econ. Geol.* 103, 1683–1690.
- Anderson, G.M., Garven, G., 1987. Sulfate-Sulfide-Carbonate Associations in Mississippi Valley-Type lead-zinc deposits. *Econ. Geol.* 82, 482–488.
- Bao, Z.A., Chen, L., Zong, C.L., Yuan, H.L., Chen, K.Y., Dai, M.N., 2017. Development of pressed sulfide powder tablets for in situ sulfur and lead isotope measurement using LA-MC-ICP-MS. *Int. J. Mass Spectrom.* 421, 255–262.
- Basoria, M.B.I., Gilbert, S., Large, R.R., Zaw, K., 2018. Textures and trace element composition of pyrite from the Bukit Botol volcanic-hosted massive sulphide deposit, Peninsular Malaysia. *J. Asian Earth Sci.* 158, 173–185.
- Canfield, D.E., 2001. Biogeochemistry of sulfur isotopes. *Stable Isotope Geochemistry* 43, 607–636.
- Canfield, D.E., Farquhar, J., 2009. Animal evolution, bioturbation, and the sulfate concentration of the oceans. *P. Natl. Acad. Sci. USA* 106, 8123–8127.
- Canfield, D.E., Teske, A., 1996. Late Proterozoic rise in atmospheric oxygen concentration inferred from phylogenetic and sulphur-isotope studies. *Nature* 382, 127–132.
- Chaussidon, M., Albarede, F., Sheppard, S.M.F., 1989. Sulphur isotope variations in the mantle from ion microprobe analyses of micro-sulphide inclusions. *Earth Planet. Sci. Lett.* 92, 144–156.
- Chen, L., Chen, K.Y., Bao, Z.A., Liang, P., Sun, T.T., Yuan, H.L., 2017. Preparation of standards for in situ sulfur isotope measurement in sulfides using femtosecond laser ablation MC-ICP-MS. *J. Anal. At. Spectrom.* 32, 107–116.
- Cook, N.J., Ciobanu, C.L., Pring, A., Skinner, W., Shimizu, M., Danyushevsky, L.V., Eidukat, B.S., Melcher, F., 2009. Trace and minor elements in sphalerite: a LA-ICPMS study. *Geochim. Cosmochim. Acta* 73, 4761–4791.
- Cooke, D.R., Bull, S.W., Large, R.R., McGoldrick, P.J., 2000. The Importance of Oxidized Brines for the Formation of Australian Proterozoic Stratiform Sediment-Hosted Pb-Zn (Sedex) Deposits. *B. Soc. Econ. Geol.* 95, 1–18.
- Corbella, M., Ayora, C., Cardellach, E., 2004. Hydrothermal mixing, carbonate dissolution and sulfide precipitation in Mississippi Valley-type deposits. *Miner. Deposita* 39, 344–357.
- Craig, J.R., Barton, P.B., 1973. Thermochemical Approximations for Sulfosal. *Econ. Geol.* 68, 493–506.
- Deng, J., Wang, Q.F., Li, G.J., Li, C.S., Wang, C.M., 2014a. Tethys tectonic evolution and its bearing on the distribution of important mineral deposits in the Sanjiang region, SW China. *Gondwana Res.* 26, 419–437.
- Deng, J., Wang, Q.F., Li, G.J., Santosh, M., 2014b. Cenozoic tectono-magmatic and metallogenetic processes in the Sanjiang region, southwestern China. *Earth Sci. Rev.* 138, 268–299.
- Eldridge, C.S., Compston, W., Williams, I.S., Harris, J.W., Bristow, J.W., Kinny, P.D., 1995. Applications of the SHRIMP 1 ion microprobe to the understanding of processes and timing of diamond formation. *Econ. Geol.* 90, 271–280.
- Feng, C.X., Bi, X.W., Hu, R.Z., Liu, S., Wu, L.Y., Tang, Y.Y., Zou, Z.C., 2011. Study on paragenesis-separation mechanism and source of ore-forming element in the Baiyangping Cu-Pb-Zn-Ag polymetallic ore deposit, Lanping basin, southwestern China. *Acta Petrologica Sinica* 27, 2609–2624 (in Chinese with English abstract).
- Feng, C.X., Bi, X.W., Liu, S., Hu, R.Z., 2014. Fluid inclusion, rare earth element

- geochemistry, and isotopic characteristics of the eastern ore zone of the Baiyangping polymetallic Ore district, northwestern Yunnan Province, China. *J. Asian Earth Sci.* 85, 140–153.
- Feng, D.X., Hu, X.C., Xiao, F.Q., Song, X.L., Xiao, B.S., Yu, X.Y., Chen, J.W., Yu, J.S., Mu, X.M., 2006. Evaluation report on Lanuoma lead-zinc polymetallic deposit, Changdu basin. Tibet, Institute of Geological Survey of Tibet Autonomous Region (in Chinese).
- Folk, R.L., 2005. Nannobacteria and the formation of framboidal pyrite: Textural evidence. *J. Earth Syst. Sci.* 114, 369–374.
- Fu, X.G., Pang, Y.C., 2004. Geological characteristics of Jinding lead-zinc deposit with discussion on its genesis. *Global Geol.* 23, 238–244 (in Chinese with English abstract).
- Gadd, M.G., Matthews, D.L., Peter, J.M., Paradis, S.J., 2016. The world-class Howard's Pass SEDEX Zn-Pb district, Selwyn Basin, Yukon. Part I: trace element compositions of pyrite record input of hydrothermal, diagenetic, and metamorphic fluids to mineralization. *Miner. Deposita* 51, 319–342.
- Garven, G., 1985. The role of regional fluid flow in the genesis of the Pine Point deposit, Western Canada sedimentary basin. *Econ. Geol.* 80, 307–324.
- Genna, D., Gaboury, D., 2015. Deciphering the Hydrothermal Evolution of a VMS System by LA-ICP-MS Using Trace Elements in Pyrite: An Example from the Bracemac-McLeod Deposits, Abitibi, Canada, and Implications for Exploration. *Econ. Geol.* 110, 2087–2108.
- Guo, L.G., Liu, Y.P., Xu, W., Zhang, X.C., Qin, K.Z., Li, T.S., Shi, Y.R., 2006. Constraints to the mineralization age of the Yulong porphyry copper deposit from SHRIMP U-Pb zircon data in Tibet. *Acta Petrological Sinica* 21, 1009–1016 (in Chinese with English abstract).
- Giordano, T.H., 2002. Transport of Pb and Zn by carboxylate complexes in basinal ore fluids and related petroleum-feld brines at 100 °C: the influence of pH and oxygen fugacity. *Geochem. T.* 3, 56–72.
- Gregory, D.D., Large, R.R., Halpin, J.A., Baturina, E.L., Lyons, T.W., Wu, S., Danyushevsky, L.V., Sack, P.J., Chappaz, A., Maslennikov, V.V., Bull, S.W., 2015. Trace Element Content of Sedimentary Pyrite in Black Shales. *Econ. Geol.* 110, 1389–1410.
- Gu, L.X., McClay, K.R., 1992. Pyrite deformation in stratiform lead-zinc deposits of the Canadian Cordillera. *Miner. Deposita* 27, 169–181.
- Guy, B.M., Ono, S., Gutzmer, J., Lin, Y., Beukes, N.J., 2014. Sulfur sources of sedimentary “buckshot” pyrite in the Auriferous Conglomerates of the Mesoarchean Witwatersrand and Ventersdorp Supergroups, Kaapvaal Craton, South Africa. *Miner. Deposita* 49, 751–775.
- He, L.Q., Chen, K.X., Wei, J.Q., Yu, F.M., 2005. Geological and geochemical characteristics and genesis of ore deposits in eastern ore belt of Baiyangping area, Yunnan Province. *Mineral Deposits* 1, 61–70 (in Chinese with English abstract).
- Hou, Z.Q., Cook, N.J., 2009. Metallogenesis of the Tibetan collisional orogen: a review and introduction to the special issue. *Ore. Geol. Rev.* 36, 2–24.
- Hou, Z.Q., Ma, H.W., Zaw, K., Zhang, Y.Q., Wang, M.J., Wang, Z., Pan, G.T., Tang, R.L., 2003. The Himalayan Yulong porphyry copper belt: product of large-scale strike-slip faulting in Eastern Tibet. *Econ. Geol.* 98, 125–145.
- Jiang, Y.H., Jiang, S.Y., Ling, H.F., Dai, B.Z., 2006. Low-degree melting of a metasomatized lithospheric mantle for the origin of Cenozoic Yulong monzogranite-porphyry, east Tibet: geochemical and Sr–Nd–Pb–Hf isotopic constraints. *Earth Planet. Sci. Lett.* 241, 617–633.
- Jørgensen, B.B., Isaksen, M.F., Jannasch, H.W., 1992. Bacterial Sulfate Reduction Above 100 °C in Deep-Sea Hydrothermal Vent Sediments. *Science* 258, 1756–1757.
- Kesle, S.E., 2005. Ore-Forming Fluids. *Elements* 1, 13–18.
- Koglin, N., Frimmel, H.E., Minter, W.E.L., Bratz, H., 2010. Trace-element characteristics of different pyrite types in Mesoarchean to Palaeoproterozoic placer deposits. *Miner. Deposita* 45, 259–280.
- Krupp, R.E., 1988. Solubility of stibnite in hydrogen sulfide solutions, speciation, and equilibrium constants, from 25 to 350 °C. *Geochem. Cosmochim. Acta* 52, 3005–3015.
- Large, R.R., Danyushevsky, L.V., Hollit, C., Maslennikov, V.V., Meffre, S., Gilbert, S., Bull, S., Scott, R.J., Emsbo, P., Thomas, H., Singh, B., Foster, J., 2009. Gold and Trace Element Zonation in Pyrite Using a Laser Imaging Technique: Implications for the Timing of Gold in Orogenic and Carlin-Style Sediment-Hosted Deposits. *Econ. Geol.* 104, 635–668.
- Large, R.R., Maslennikov, V.V., Robert, F., Danyushevsky, L.V., Chang, Z.S., 2007. Multistage Sedimentary and Metamorphic Origin of Pyrite and Gold in the Giant Sukhoi Log Deposit, Lena Gold Province, Russia. *Econ. Geol.* 102, 1233–1267.
- Li, C., Xie, L.W., Dong, Y.S., Qiangba, Z.X., Jiang, G.W., 2009. Discussion on the age of Jitang Group around Leiwuqi area, eastern Tibet, China and primary understanding. *Geological Bulletin of China* 28, 1178–1180 (in Chinese with English abstract).
- Li, X.H., Fan, H.R., Yang, K.F., Hollings, P., Liu, X., Hu, F.F., Cai, Y.C., 2018. Pyrite textures and compositions from the Zhuangzi Au deposit, southeastern North China Craton: implication for ore-forming processes. *Contrib. Mineral. Petrol.* 173, 72–91.
- Liu, Y.C., Hou, Z.Q., Yu, Y.S., Tian, S.H., Li, Y.L., Yang, Z.S., 2013. Characteristics and genesis of Lalongla MVT-like deposit in Changdu region. Tibet. *Acta Petrological Sinica* 29, 1407–1426 (in Chinese with English abstract).
- Liu, Y.C., Kendrick, M.A., Hou, Z.Q., Yang, Z.S., Tian, S.H., Song, Y.C., Honda, M., 2017. Hydrothermal Fluid Origins of Carbonate-Hosted Pb-Zn Deposits of the Sanjiang Thrust Belt, Tibet: Indications from Noble Gases and Halogens. *Econ. Geol.* 112, 1247–1268.
- Ma, Q.S., Ellis, G.S., Amrani, A., Zhang, T.W., Tang, Y.C., 2008. Theoretical study on the reactivity of sulfate species with hydrocarbons. *Geochem. Cosmochim. Acta* 72, 4565–4576.
- Machel, H.G., 2001. Bacterial and thermochemical sulfate reduction in diagenetic settings - old and new insights. *Sediment. Geol.* 140, 143–175.
- Machel, H.G., Krouse, H.R., Sassen, R., 1995. Products and distinguishing criteria of bacterial and thermochemical sulfate reduction. *Appl. Geochem.* 10, 373–389.
- Maslennikov, V.V., Maslennikova, S.P., Large, R.R., Danyushevsky, L.V., 2009. Study of Trace Element Zonation in Vent Chimneys from the Silurian Yaman-Kasy Volcanic-Hosted Massive Sulfide Deposit (Southern Urals, Russia) Using Laser Ablation-Inductively Coupled Plasma Mass Spectrometry (LA-ICPMS). *Econ. Geol.* 104, 1111–1141.
- Mei, Y., Sherman, D.M., Liu, W.H., Etschmann, B., Testemale, D., Brugger, J., 2015. Zinc complexation in chloride-rich hydrothermal fluids (25–600 °C): a thermodynamic model derived from ab initio molecular dynamics. *Geochem. Cosmochim. Acta* 150, 265–284.
- Meshoulam, A., Ellis, G.S., Ahmad, W.S., Deev, A., Sessions, A.L., Tang, Y.C., Adkins, J.F., Liu, J.Z., Gilhooly, W.P., Aizenshtat, Z., Amrani, A., 2016. Study of thermochemical sulfate reduction mechanism using compound specific sulfur isotope analysis. *Geochem. Cosmochim. Acta* 188, 73–92.
- O’Neil, J.R., 1986. Theoretical and experimental aspects of isotopic fractionation. *Rev. Mineral. Geochem.* 16, 1–40.
- Obolensky, A.A., Gushchina, L.V., Borisenko, A.S., Borovikov, A.A., Pavlova, G.G., 2007. Antimony in hydrothermal processes: solubility, conditions of transfer, and metal-bearing capacity of solutions. *Russ. Geol. Geophys.* 48, 992–1001.
- Ohmoto, H., 1972. Systematics of Sulfur and Carbon Isotopes in Hydrothermal Ore Deposits. *B. Soc. Econ. Geol.* 67, 551–578.
- Ohmoto, H., Rye, R.O., 1979. Isotopes of sulfur and carbon. In: Barnes, H.L. (Ed.), *Geochemistry of Hydrothermal Ore Deposits*. Wiley, New York, pp. 509–567.
- Olson, R.A., 1984. Genesis of paleoarkar and strata-bound zinc-lead sulfide deposits in a Proterozoic dolostone, northern Baffin Island, Canada. *Econ. Geol.* 79, 1056–1103.
- Peng, Y.M., Chen, F.Z., Wang, L.Q., 1997. Gaoji alkaline rock body in the Changdu basin in the Nujiang-Lancangjiang-Jinshajiang area. *Tethyan Geol.* 21, 100–109 (in Chinese with English abstract).
- Pokrovski, G.S., Borisova, A.Y., Roux, J., Hazemann, J.L., Petdang, A., Tella, M., Testemale, D., 2006. Antimony speciation in saline hydrothermal fluids: a combined X-ray absorption fine structure spectroscopy and solubility study. *Geochem. Cosmochim. Acta* 70, 4196–4214.
- Raiswell, R., Plant, J., 1980. The Incorporation of Trace Elements into Pyrite during Diagenesis of Black Shales, Yorkshire. *Englan. Econ. Geol.* 75, 684–699.
- Reich, M., Deditius, A., Chrysosoulis, S., Li, J.W., Ma, C.Q., Parada, M.A., Barra, F., Mittermayr, F., 2013. Pyrite as a record of hydrothermal fluid evolution in a porphyry copper system: a SIMS/EMPA trace element study. *Geochem. Cosmochim. Acta* 104, 42–62.
- Schieber, J., 2002. Sedimentary pyrite: A window into the microbial past. *Geology* 30, 531–534.
- Seal II, R.R., 2006. Sulfur Isotope Geochemistry of Sulfide Minerals. *Rev. Mineral. Geoch.* 61, 633–677.
- Seal II, R.R., Alpers, C.N., Rye, R.O., 2000. Stable Isotope Systematics of Sulfate Minerals. *Rev. Mineral. Geoch.* 40, 541–602.
- Sverjensky, D.A., 1981. The Origin of a Mississippi Valley-Type Deposit in the Viburnum Trend, Southeast Missouri. *Econ. Geol.* 76, 1848–1872.
- Sverjensky, D.A., 1986. Genesis of Mississippi Valley-Type Lead-Zinc Deposits. *Ann. Rev. Earth Planet. Sci.* 1986 (14), 177–199.
- Symons, D.T.A., Lewchuk, M.T., Kawasaki, K., Velasco, F., Leach, D.L., 2009. The Reocin zinc-lead deposit, Spain: paleomagnetic dating of a late Tertiary ore body. *Mineral. Deposita* 44, 867–880.
- Tagirov, B.R., Seward, T.M., 2010. Hydrosulfide/sulfide complexes of zinc to 250 °C and the thermodynamic properties of sphalerite. *Chem. Geol.* 269, 301–311.
- Tang, J.X., Zhong, K.H., Liu, Z.C., Li, Z.J., Dong, S.Y., Zhang, L., 2006. Intracontinent orogen and metallogenesis in Himalayan epoch Changdu Large Composite Basin, Eastern Tibet. *Acta Geological Sinica* 80, 1364–1376 (in Chinese with English abstract).
- Tang, Y.Y., Bi, X.W., Fayek, M., Hu, R.Z., Wu, L.Y., Zhi, Z.C., Feng, C.X., Wang, X.S., 2014. Microscale sulfur isotopic compositions of sulfide minerals from the Jinding Zn-Pb deposit, Yunnan Province, Southwest China. *Gondwana Res.* 26, 594–607.
- Tang, Y.Y., Bi, X.W., Fayek, M., Stuart, F.M., Wu, L.Y., Jiang, G.H., Xu, L.L., Liang, F., 2017. Genesis of the Jinding Zn-Pb deposit, northwest Yunnan Province, China: constraints from rare earth elements and noble gas isotopes. *Ore. Geol. Rev.* 90, 970–986.
- Tao, Y., Bi, X.W., Li, C.S., Hu, R.Z., Li, Y.B., Liao, M.Y., 2014. Geochronology, petrogenesis and tectonic significance of the Jitang granitic pluton in eastern Tibet, SW China. *Lithos* 184, 214–323.
- Tao, Y., Bi, X.W., Xin, Z.L., Zhu, F.L., Liao, M.Y., Li, Y.B., 2011. Geology, geochemistry and origin of Lanuoma Pb-Zn-Sb deposit in Changdu area, Tibet. *Mineral Deposits* 4, 599–615 (in Chinese with English abstract).
- Thode, H.G., Monster, J., Dunford, H.B., 1961. Sulphur isotope geochemistry. *Geochem. Cosmochim. Acta* 25, 150–174.
- Torssander, P., 1989. Sulfur isotope ratios of Icelandic rocks. *Contrib. Mineral. Petrol.* 102, 18–23.
- Ulrich, T., Long, D.G.F., Kamber, B.S., Whitehouse, M.J., 2011. In Situ Trace Element and Sulfur Isotope Analysis of Pyrite in a Paleoproterozoic Gold Placer Deposit, Pardo and Clement Townships, Ontario, Canada. *Econ. Geol.* 106, 667–686.
- Velasco, F., Herrero, J.M., Yusta, I., Alonso, J.A., Seebold, I., Leach, D.L., 2003. Geology and Geochemistry of the Reocin Zinc-Lead Deposit, Basque-Cantabrian Basin, Northern Spain. *Econ. Geol.* 98, 1371–1396.
- Wang, C.M., Bagas, L., Lu, Y.J., Santosh, M., Du, B., McCuaig, T.C., 2016. Terrane boundary and spatio-temporal distribution of ore deposits in the Sanjiang Tethyan Orogen: insights from zircon Hf-isotopic mapping. *Earth Sci. Rev.* 156, 39–65.
- Wang, X.H., Hou, Z.Q., Song, Y.C., Zhang, H.R., 2015. Geological, fluid inclusion and isotopic studies of the Baiyangping Pb–Zn–Cu–Ag polymetallic deposit, Lanping basin, Yunnan province, China. *J. Asian Earth Sci.* 111, 853–871.
- Wang, X.H., Song, Y.C., Hou, Z.Q., Zhang, H.R., Wang, Z., Zhuang, T.M., Zhang, C.,

- Zhang, T.F., 2011. Geological characteristics of the Baiyangping Pb-Zn-Cu-Ag polymetallic deposit in northern Lanping basin. *Acta Petrological et Mineralogical* 30, 507–518 (in Chinese with English abstract).
- Warren, J.K., 1999. *Evaporites: Their Evolution and Economics*. Blackwell Scientific Publication, Oxford.
- Wen, H.J., Zhu, C.W., Zhang, Y.X., Cloquet, C., Fan, H.F., Fu, S.H., 2016. Zn/Cd ratios and cadmium isotope evidence for the classification of lead-zinc deposits. *Sci. Rep.* 6, 1–8.
- Wilkin, R.T., Barnes, H.L., Brantley, S.L., 1996. The size distribution of framboidal pyrite in modern sediments: an indicator of redox conditions. *Geochim. Cosmochim. Acta* 60, 3897–3912.
- Williams-Jones, A.E., Normand, C., 1997. Controls of Mineral Parageneses in the System Fe-Sb-S-O. *Econ. Geol.* 92, 308–324.
- Wood, S.A., Crerar, D.A., Borcsik, M.P., 1987. Solubility of the assemblage pyrite-pyrhotite-magnetite-sphalerite galena-gold-stibnite-bismuthinite-argentite-molybdenite in H₂O-NaCl-CO₂ Solutions from 200 °C to 350 °C. *Econ. Geol.* 82, 1864–1887.
- Xu, C.X., 2017. Geochemical features and ore genesis of sediment-hosted lead-zinc deposits in the Changdu area, Tibet-exemplified by Lanuoma and Cuona Pb-Zn deposits [Ph.D. thesis]: Guiyang, China, Institute of Geochemistry, Chinese Academy of Sciences 68–69 (in Chinese with English abstract).
- Xu, C.X., Yin, R.S., Peng, J.T., Hurley, J.P., Lepak, R.F., Gao, J.F., Feng, X.B., Hu, R.Z., Bi, X.W., 2018. Mercury isotope constraints on the source for sediment-hosted lead-zinc deposits in the Changdu area, southwestern China. *Miner. Deposita* 53, 339–352.
- Xue, C.J., Zeng, R., Liu, S.W., Chi, G.X., Qing, H.R., Chen, Y.C., Yang, J.M., Wang, D.H., 2007. Geologic, fluid inclusion and isotopic characteristics of the Jinding Zn-Pb deposit, western Yunnan, South China: a review. *Ore. Geol. Rev.* 31, 337–359.
- Yalikun, Y., Xue, C.J., Symons, D.T.A., 2018. Paleomagnetic age and tectonic constraints on the genesis of the giant Jinding Zn-Pb deposit, Yunnan, China. *Miner. Deposita* 53, 245–259.
- Yan, J., Hu, R.Z., Liu, S., Lin, Y.T., Zhang, J.C., Fu, S.L., 2018. NanoSIMS element mapping and sulfur isotope analysis of Au-bearing pyrite from Lannigou Carlin-type Au deposit in SW China: New insights into the origin and evolution of Au-bearing fluids. *Ore. Geol. Rev.* 92, 29–41.
- Yardley, B.W.D., 2005. Metal concentrations in crustal fluids and their relationship to ore formation. *Econ. Geol.* 100, 613–632.
- Ye, L., Cook, N.J., Giobanu, C.L., Liu, Y.P., Zhang, Q., Liu, T.G., Gao, W., Yang, Y.L., Danyushevsky, L.V., 2011. Trace and minor elements in sphalerite from base metal deposits in South China: a LA-ICPMS study. *Ore. Geol. Rev.* 39, 188–217.
- Zhang, J.C., Lin, Y.T., Yang, W., Shen, W.J., Hao, J.L., Hua, S., Cao, M.J., 2014. Improved precision and spatial resolution of sulfur isotope analysis using NanoSIMS. *J. Anal. At. Spectrom.* 29, 1934–1943.
- Zhong, R.C., Brugger, J., Chen, Y.J., Li, W.B., 2015. Contrasting regimes of Cu, Zn and Pb transport in ore-forming hydrothermal fluids. *Chem. Geol.* 395, 154–164.